

1 **Spatiotemporal mapping of invasive yellow sweetclover blooms using Sentinel-2 and high-
2 resolution drone imagery**

3
4 Sakshi Saraf^{1,*}, Ranjeet John^{1,2}, Venkatesh Kolluru², Khushboo Jain², Geoffrey Henebry^{3,4}, Jiquan
5 Chen^{3,4}, Raffaele Laforteza⁵

6
7 *Corresponding author: Sakshi Saraf; Email: Sakshi.Saraf@coyotes.usd.edu; Orcid: 0000-0002-6785-
8 8381

9
10 1. Department of Biology, University of South Dakota, Vermillion, SD 57069, USA
11 2. Department of Sustainability and Environment, University of South Dakota, Vermillion, SD 57069,
12 USA
13 3. Department of Geography, Environment, and Spatial Sciences, Michigan State University, East
14 Lansing, MI 48824, USA
15 4. Center for Global Change and Earth Observations, Michigan State University, East Lansing, MI 48823,
16 USA
17 5. Department of Soil, Plant and Food Sciences (DISSPA), University of Bari “Aldo Moro”, Via
18 Amendola 165/A, 70126, Bari, Italy
19
20

21 **Abstract**

22 Yellow sweetclover (*Melilotus officinalis* (L.) Lam.; MEOF) is an invasive forb pervasive across
23 the Northern Great Plains in the United States, often linked to traits such as wide adaptability,
24 strong stress tolerance, and high productivity. Despite MEOF's prevalent ecological-economic
25 impacts and importance, knowledge of its spatial distribution and temporal evolution is
26 extremely limited. Here, we aim to develop a spatial database of annual MEOF abundance
27 (2016-2023) across western South Dakota (SD) at 10 m spatial resolution by applying a
28 generalized prediction model on Sentinel-2 imagery. We collected *in situ* quadrat-based total
29 vegetation cover with MEOF percent cover estimates across western SD from 2021 through
30 2023 and synthesized with other available percent cover estimates (2016-2022) of several
31 federal, state, and non-governmental sources. We conducted drone overflights at 14 sites across
32 Butte County, SD in 2023 to develop very high spatial resolution (4-6 cm) and accurate MEOF
33 cover maps by applying a random forest (RF) classification model. The field-measured and
34 uncrewed aerial system (UAS) derived MEOF percent cover estimates were used to train, test,
35 and validate a RF regression model. The predicted MEOF percent cover dataset was validated
36 with UAS-derived percent cover in 2023 across four sites (out of 14 sites). We found that the
37 variation in the Normalized Difference Moisture Index and Distance to roads were among the top
38 predicting variables in predicting MEOF abundance. Our predictive model yielded greater
39 accuracies with an R² of 0.76, RMSE of 15.11%, MAE of 10.95%, and MAPE of 1.06%. We
40 further validated our 2023 predicted maps using the 3-m resolution PlanetScope imagery for
41 regions where field samples could not be collected in 2023. The database of MEOF abundance
42 showed consecutive years of average or above-average precipitation yielded a higher MEOF
43 abundance across the study region. The database could assist local land managers and
44 government officials pinpoint locations requiring timely land management to control the rapid
45 spread of MEOF in the Northern Great Plains. The developed invasive MEOF percent cover
46 datasets are freely available at the figshare repository
47 (<https://doi.org/10.6084/m9.figshare.29270759.v1>).

48
49 Keywords: Invasive, UAV, random forest, Planet imagery, Yellow sweetclover

50 **1. Introduction**

51
52 Invasive plant species pose severe threat on ecosystem structure and functions (Rai and Singh,
53 2020). In particular, the Northern Great Plains (NGP) grasslands in the United States are being
54 threatened by long-established and newly arrived invasive plant species and loss of diversity
55 (Hendrickson et al., 2019). These invasive species compete against native species, diminishing
56 ecological goods and services and degrade vulnerable grassland ecosystems (Gaskin et al.,
57 2021). Furthermore, the ecosystem responses of grasslands in general including NGP are
58 becoming increasingly variable in space and time due to the myriad influences from climate
59 change (Bernath-Plaisted et al., 2023; Cleland et al., 2013; Zhang et al., 2022). These conditions
60 accelerate and contribute to the difficult to predict dynamics of invasive plant species that often
61 are spread unintentionally (Spiess et al., 2020). The NGP comprises public, tribal, and private
62 lands, resulting in a patchwork of management goals and invasive plant control strategies
63 (Langholz, 2010). Ecological studies that operate within restricted spatial boundaries or plot-
64 based datasets are advantageous in providing comprehensive insights into local invasion
65 scenarios (Martins et al., 2016). However, previous studies often lack important spatiotemporal
66 data on invasion dynamics, such as changes in species cover, spread rates, and environmental
67 drivers, making it difficult to fully understand invasion processes that unfold continuously across
68 space and time (Larson et al., 2020). Developing timely updates of the spatial and temporal
69 spread of invasive plant species therefore have been increasingly urged to effectively and
70 efficiently address the challenges posed by invasive species in changing habitats is an urgent
71 need (Van Rees et al., 2022).

72
73 In general, understanding the spatio-temporal patterns of a biennial plant species that are either
74 ephemeral in nature or bloom in specific years is challenging due to their phenological cycle.
75 Yellow sweetclover (*Melilotus officinalis* (L.) Lam., MEOF), a common invasive legume in the
76 NGP, exemplifies this biennial phenology. There has been little to no literature on mapping
77 blooms of such plant species until the 2010s. In recent years, MEOF has attracted attention from
78 land managers in South Dakota (SD) as it is becoming a prominent invasive species in the NGP
79 region. We refer to years with MEOF super blooms (Preston et al., 2023) in the Dakota region as
80 "sweetclover years". MEOF is a nitrogen-fixing, biennial legume forb native to Eurasia (Luo et
81 al., 2016). It has noticeable pea-like, strongly scented yellow flowers arranged in a narrow
82 raceme, which can grow more than 4 cm long (Varner, 2022). The ability of MEOF to establish
83 and grow in a wide range of temperature, precipitation, and soil conditions has naturalized its
84 presence in the NGP region (Kan et al., 2023). It is often one of the first plants to appear in
85 disturbed or open sites, including pastures, agricultural fields, roadsides, rangelands, and open
86 slopes in badlands, prairies, or floodplains (Wolf et al., 2003).

87
88 Invasive forbs such as MEOF develop yellow inflorescences that are prominent during flowering
89 time and can be detected using 10 m resolution Sentinel-2 derived reflectance and quantitative
90 indices, provided the plants meet the optimal size or developmental stage for detection (Saraf et
91 al., 2023). Previous studies have shown that multi-temporal analysis using remote sensing data
92 can be a powerful tool for addressing challenges in monitoring invasive species dynamics

93 (Bradley, 2014; Mouta et al., 2023). For example, Sentinel-2 imagery with 10 m spatial
94 resolution has sufficed for mapping a range of invasive plant species (Kattenborn et al., 2019). In
95 addition, the high temporal resolution of the Sentinel-2 can help capture phenological
96 characteristics and identify species with pronounced flowering periods. However, there have
97 been relatively very few efforts to map MEOF in the NGP due, in part, to its unreliable annual
98 aboveground establishment resulting in low to moderate abundance during drier years
99 complicating attempts to map its distribution. Moreover, its yellow flowers can be easily
100 mistaken in remote sensing imagery for other yellow-flowered forbs such as yellow salsify, black
101 eyed susan, western wallflower, annual sunflower or leafy spurge. MEOF tends to grow in dense
102 patches and invade vast areas with the capability of growing up to 2 m tall when ample moisture
103 is available during its growth period. In the recent wet year of 2019, MEOF thrived across the
104 NGP, resulting in minimal spatial overlaps with other yellow flowered plants and enabling
105 researchers to map its spatial distribution. Specific years with an enhanced bloom of MEOF, such
106 as 2019 and 2023, were easily distinguished in image time series due to their extensive spread,
107 tall canopy, and prolific yellow flowers during summer (Preston et al., 2023). Such climate
108 conditions create an opportunity to collect more ground samples to increase accurate mapping of
109 MEOF distribution.

110
111 In traditional remote sensing, *in situ* reference data are required to detect and validate complex
112 patterns and ecologically relevant processes (Mayr et al., 2019). The reference data collection is
113 usually labor-intensive, time-consuming, and logistically difficult across large spatial areas.
114 Uncrewed Aerial Systems (UAS), combined with high-resolution multispectral or hyperspectral
115 cameras, offer a promising, user-friendly, and low-cost alternative data source to *in situ* data
116 collection (Horstrand et al., 2019; Li and Tsai, 2017; Rakotoarivony et al., 2023). Despite the
117 limited spatial extent of each swatch, UAS still enables the acquisition of spatially continuous
118 information on species cover with ultra-high spatial resolution (e.g., ground sampling distance of
119 <10 cm) and temporal flexibility (Turner and Wallace, 2013). Numerous studies have
120 demonstrated the potentials of UAS data as an alternative source to supplement or even replace
121 the traditional sampling methods of detecting species presence in the field (Alvarez-Taboada et
122 al., 2017; Baena et al., 2017; Kattenborn et al., 2019). UAS data can be used to train models that
123 employ fine-to-medium spatial resolution data, such as Sentinel-2 imagery, to map invasives at
124 regional scales (Preston et al., 2023), despite a small survey extent (Colomina and Molina,
125 2014).

126
127 Previously, we lacked sufficient statistical power and comprehensive spatial coverage due to
128 small sample size to conduct regional scale mapping for the 2019 MEOF blooms (Saraf et al.,
129 2023). Preston et al., (2023) used an ensemble of MaxEnt models to map MEOF fractional cover
130 for 2019 using UAS data at 16 sites across three counties in SD and Montana using satellite
131 imagery trained from regional UAS imageries. Our team also examined the contribution of
132 various biophysical factors to MEOF and tested different machine learning algorithms to
133 determine the best algorithm to map the MEOF for 2019 (Saraf et al., 2023). We found that the
134 random forest (RF) algorithm (Breiman et al., 1984) outperformed other machine learning
135 algorithms in mapping the distribution of invasive MEOF cover. However, our results also

136 indicated a significant underestimation of the percent cover due to the limited sample size. We,
137 therefore, aimed to increase the sampling size by collecting quadrat-based percent cover and
138 UAS imagery over MEOF blooms and synthesizing estimates from various state and federal
139 sources to overcome uncertainties and the limitation of underestimation.

140
141 We endeavored to optimize the utilization of UAS and Sentinel-2 data to create a reference
142 percent cover dataset, which was then used as a training and validation inputs for a RF modeling
143 framework. This approach helped develop an annual time-series percent cover database for the
144 invasive MEOF. Developing a generalized model that can be applied across space and time
145 allows for efficient mapping of irruptive invasive plant species, which often bloom episodically
146 and occur in clustered patches. Such distributions are often underrepresented in conventional
147 field survey datasets, including our ground reference data, because random sampling rarely
148 captures them adequately. Effective management of plant invasives such as MEOF will require
149 spatially continuous, multitemporal maps of species occurrence and cover as its first step.
150 Building such a database for invasive MEOF can help to comprehend the spatial and temporal
151 dynamics of its invasion patterns (Müllerová et al., 2017). Therefore, our objectives are
152 threefold: (1) to develop a generalized prediction model using field-collected and UAS-derived
153 percent cover samples along with Sentinel 2 imagery to map the fractional cover of invasive
154 MEOF across western SD; (2) to compare and validate our model-derived percent cover
155 estimates against the drone-derived estimates; and (3) to further validate the predicted yellow
156 sweetclover maps using PlanetScope imagery, which provides higher temporal resolution and
157 independent data for cross-sensor validation, and to assess MEOF cover in regions lacking UAS
158 coverage. We ask two research questions. First, what are the spatiotemporal distributions of
159 invasive MEOF across western SD? Second, are the spatiotemporal distributions of MEOF
160 explained by precipitation in bloom years? For land managers, it is crucial to both understand
161 the current distribution of MEOF in recent years and appreciate its invasion dynamics, to curb
162 further spread of MEOF into previously unaffected areas. The developed invasive species cover
163 database would therefore help to design mitigation strategies effectively and promote the
164 proactive conservation of grassland ecosystems.

165

166 2. Methods

167

168 2.1 Study Area

169

170 Western SD is located within the Upper Missouri River Basin and is a part of the NGP,
171 characterized by the Black Hills along with prairie at the southwestern corner, along with high
172 buttes, canyons, and wide expanses of nearly level tablelands (Figure 1). This region experiences
173 a semi-arid climate with high interannual variability in precipitation, averaging around 300-400
174 mm (Agnew et al., 1986). About three-fourths of the precipitation occurs during summer, and
175 snowfall ranges from 650 mm to 5000 mm throughout western SD (Paul et al., 2016). Despite
176 the substantial conversions of rangeland to cultivated lands in the U.S. Midwest, most of the
177 central and western SD landscapes are still dominated by rangelands. The landscape of western
178 SD is a mosaic of mixed-grass prairie interspersed with cultivated lands. The mixed grass prairie

shifts into shortgrass and sagebrush grassland in the extreme western portion of the state. The dominant grasses include western wheatgrass (*Pascopyrum smithii* (Rydb.) Á. Löve), needle and thread (*Hesperostipa comata* (Trin. & Rupr.) Barkworth), little bluestem (*Schizachyrium scoparium* (Michx.) Nash), prairie sandreed (*Calamovilfa longifolia* (Hook.) Scribn), green needlegrass (*Nassella viridula* (Trin.) Barkworth), blue grama (*Bouteloua gracilis* (Willd. ex Kunth.) Lag. ex Griffiths) and threadleaf sedge (*Carex filifolia* Nutt.). Dryland sedges (*Carex* spp. L.), prairie threeawn (*Aristida oligantha* Michx.), and fringed sagewort (*Artemisia frigida* Willd.) increase with disturbance (Owensby and Launchbaugh, 1977; Reinhart et al., 2019; Sanderson et al., 2015). Several perennial forbs such as western wallflower (*Erysimum asperum* (Nutt.) DC.), Canada thistle (*Cirsium arvense* (L.) Scop.)), leafy spurge (*Euphorbia esula* L.), purple prairie clover (*Dalea purpurea* Vent. var. *purpurea*) and shrubs such as big sagebrush (*Artemisia tridentata* Nutt.), broom snakeweed (*Gutierrezia sorothrae* Pursh) and leadplant (*Amorpha canescens* Pursh) are prevalent. The most common invasive grasses include Kentucky bluegrass (*Poa pratensis* L.), smooth brome (*Bromus inermis* Leyss.), cheatgrass (*Bromus tectorum* L.), and curlycup gumweed (*Grindelia squarrosa* (Pursh) Dunal). Yellow salsify (*Tragopogon dubius* Scop.) and yellow sweetclover (*Melilotus officinalis* (L.) Lam.) are common invasive annual-biennial forbs in this region (Johnson and Larson, 1999).

196 197 2.2 UAS Survey 198

199 Ultra-high spatial resolution UAS imagery were acquired for 14 sites during a field campaign
200 from July 9 to July 15, 2023. The flight locations were randomly selected across Butte County in
201 western South Dakota to capture large, continuous patches of MEOF, ensuring that the imagery
202 encompassed the full range of percent cover within each site, including areas without MEOF. We
203 collected multispectral (Visible, RedEdge, and Near InfraRed) imagery using a MicaSense
204 RedEdge-MX (MicaSense, 2015) camera deployed on a DJI Matrice 200 UAS platform. The
205 radiometric calibration of the sensor was implemented by converting the digital values of the
206 orthomosaic to the values of surface spectral reflectance by Micasense calibration panel. The
207 area covered for each flight ranged between 1 ha and 10 ha, depending on the patch size of the
208 MEOF invasion (Table S7). The imagery was captured with at least 80% forward and 75% side
209 overlap (Table 1). We flew the flight at an average altitude of 30-60 m above ground, ensuring a
210 spatial resolution of at least 3 cm. We used the recorded inertial measuring unit (IMU) and
211 Global Navigation Satellite System (GNSS) module of the UAS along with Real-Time
212 Kinematic (RTK) positioning (~1 cm accuracy) to guide the drone by placing four Ground
213 Control Points (GCPs) at each site to ensure the geometric accuracy of the images taken by the
214 drone matched the Sentinel-2 imagery. Several studies have demonstrated that using GCPs can
215 lead to higher accuracies in the processed orthoimages than direct georeferencing (Jurjević et al.,
216 2020; Padró et al., 2019). Moreover, GCPs help advance the upscaling of UAS to Sentinel-2
217 imagery with the best alignment and minimum shift (Gränzig et al., 2021). Therefore, we
218 processed the UAS images in Pix4D mapper (Pix4D S.A., 2022), and georeferenced the
219 orthomosaics using the GPS coordinates of plot center and corner targets collected with Trimble
220 Catalyst DA2 GNSS receiver kit (Trimble Inc. (n.d.), 2025) with a precision level of 1 cm
221 accuracy. All 14 sites captured the observed range of MEOF percent cover, but they differed in
222 total area covered by MEOF presence and the number of samples derived from each site. To
223 ensure a balanced split, the 10 smaller sites were randomly selected for training the RF model,

224 while the remaining four larger sites were reserved for validation. This approach ensured that
225 both the training and validation sets contained approximately equal numbers of samples,
226 providing an unbiased assessment of model performance.

227
228 2.3 Field measurements and sample collection
229

230 We used a total of 22,972 MEOF percent cover samples collected across western South Dakota
231 rangelands and surrounding regions during 2016–2023 (Table S1). This included 5,283 samples
232 derived from UAS imagery collected during the peak blooming months (June–August) in 2023
233 (details in Sections 2.2 and 2.4) across western South Dakota rangelands. In addition, 17,689
234 MEOF cover samples were retrieved and synthesized from multiple federal, state, and non-
235 governmental sources for 2016–2022 across four states: South Dakota, North Dakota, Montana,
236 and Wyoming (Figure 1a; Table S1). Although the historical samples were obtained using
237 different field protocols, they were integrated with our field-collected data to increase spatial and
238 temporal coverage. These sources included RCMAP data from the USGS Center for Earth
239 Resources Observation & Science, USGS Northern Rocky Mountain Science Center (Montana),
240 the Bureau of Land Management (BLM) database, the Northern Great Plains Inventory &
241 Monitoring Network, the National Ecological Observatory Network (NEON), and the Montana
242 Natural Heritage Program. The source, year-wise distribution, and frequency of the samples are
243 summarized in Tables S2 and S3. At the 10 m mapping scale, this compilation provided a
244 suitable reference for model training and validation. Our field-collected surveys recorded the
245 plant species composition, including dominant species and percent cover of all species present,
246 using the conventional plot-based quadrat method. Within each 30 m × 30 m plot, a minimum of
247 three 0.5 m × 0.5 m quadrats were sampled. Percent cover for each plot was calculated as the
248 average of the quadrat measurements, with each quadrat considered representative of its portion
249 of the plot. Within each quadrat, we estimated percent cover of MEOF by averaging the grids it
250 occupied, allowing fine-resolution observations to be scaled up to the plot level while capturing
251 spatial variability (John et al., 2018). We recorded flowering and non-flowering MEOF
252 individuals separately. The separation was done to document phenological variability and
253 population structure, which can be useful for understanding interannual flowering dynamics in
254 future analyses. However, only the flowering MEOF percent cover was used for remote sensing-
255 based mapping, as flowering individuals exhibit a distinct spectral signal that can be consistently
256 detected in aerial and satellite imagery. This approach ensured that the satellite-derived cover
257 estimates corresponded specifically to the detectable, flowering component of MEOF. For 2023,
258 the GPS locations of the field-collected quadrat samples were utilized as the ground control
259 points for enhancing the processing of drone imagery to derive percent cover samples.

260
261 2.4 UAS derived yellow sweetclover cover
262

263 MEOF is prominently visible in orthomosaics using a combination of green, green, and blue
264 bands. This prominence occurs because yellow flowers of MEOF increase reflectance of green
265 while slightly decreasing reflectance of blue color (Sulik and Long, 2016). We first visually
266 delineated several polygons of MEOF on the georeferenced orthomosaics using these band
267 combinations. We then used 3000 absence and 3000 presence samples derived from these

268 polygons to train a machine learning classification model and classify MEOF presence pixels
269 from other land cover pixels. We used five spectral bands (Blue, Green, Red, RedEdge, and NIR)
270 and the Normalized Difference Yellowness Index (NDYI) to classify the yellow-flowered
271 blooms in the imagery. The equation for NDYI is provided in Table S4. We implemented an RF
272 classification model on randomly split 80:20 ratio samples to segregate MEOF pixels from other
273 pixels. We tuned the RF hyperparameters ($mtry = 4$, $ntrees = 1500$) to optimize model predictive
274 performance, specifically by minimizing the Root Mean Square Error (RMSE) using 10-fold, 5-
275 repeat cross-validation. We assessed model efficiency both visually, using green–green–blue
276 false color composites, and quantitatively, by calculating Overall Accuracy and the Kappa
277 coefficient (Landis and Koch, 1977). We converted the continuous RF predictions to binary
278 presence/absence using a threshold of 0.5, assigning pixels with predicted probability ≥ 0.5 as
279 MEOF presence (assigned as 1) and pixels < 0.5 as absence (assigned as 0) (Josso et al., 2023;
280 Steen et al., 2021). We calculated the area-based weighted average of MEOF classified pixels
281 from the total number of pixels within a 10m pixel to derive MEOF percent cover at 10 m
282 resolution. The percent cover of MEOF within each 10 m resolution pixel was calculated as the
283 proportion of classified MEOF pixels within that 10 m area.

284

285 We collected and averaged minimum of three field samples per 30 m \times 30 m plot at each drone
286 site in 2023. Overall, we had 30 observed percent cover samples collected across 14 drone sites.
287 We employed a jackknife resampling procedure using leave-one-out cross-validation to calibrate
288 RF classification-derived percent cover estimates of MEOF against field-observed percent cover
289 values. For each iteration, one observation was excluded from the dataset, and a linear regression
290 model was fitted using the remaining field samples. The excluded field observation was then
291 predicted using the fitted model, based solely on its derived cover value. This process was
292 repeated for all observations, resulting in a set of cross-validated predictions for the entire
293 dataset. Calibration accuracy was assessed by comparing predicted and observed values using
294 root mean square error (RMSE) and the correlation coefficient of determination (R^2). We used
295 linear regression to calibrate RF-derived percent cover estimates because it provides a simple
296 and transparent way to correct systematic biases. To ensure unbiased predictions and minimize
297 overfitting, we applied a leave-one-out jackknife procedure, where each observation was
298 predicted independently of the data used to fit the model (Wolter, 2007). We then combined field
299 and UAS-derived samples from 2016–2023, resulting in a total of 22,972 MEOF percent cover
300 samples for the regional-scale regression analysis described in Section 2.6 and shown in Figure
301 2.

302

303 2.5 Satellite-derived predictor variables

304

305 We obtained 64 predictor variables with spatial resolutions ranging between 10 m and 1 km. We
306 derived maximum value composites of various indices and tasseled caps for the peak summer
307 months with a maximum of 10% cloud cover to enhance the spectral information of the Sentinel
308 2A imagery (Table S4) (Gascon et al., 2017). We also derived the coefficient of variation
309 (standard deviation/mean) composites to represent the variability of the indices or the tasseled
310 cap components across the summer months. For variables affected by high cloud cover or limited
311 image availability in the seasonal composites, we used the standard deviation as an alternative to
312 the coefficient of variation.

313

314 For climate predictors, we utilized the Daymet monthly and annual dataset (Version 4R1)
315 available at 1 km spatial resolution (Thornton et al., 2022). From the monthly data, we calculated
316 mean annual precipitation (MAP) as the sum of monthly precipitation values and mean annual
317 temperature (MAT) as the average of the monthly mean temperatures for each year
318 corresponding to the MEOF cover samples. To account for potential biennial effects, we also
319 calculated biennial precipitation (MAP2) and biennial temperature (MAT2) by combining the
320 values from the sample year with those of the preceding year (e.g., total precipitation across both
321 years and average temperature across both years). We also computed seasonal composites of
322 precipitation and mean temperature for each year separately corresponding to the MEOF cover
323 samples, including spring (March–May; P_MAM and T_MAM) and summer (June–August;
324 P_JJA and T_JJA). We acquired percent snow cover at 500m resolution from the MODerate
325 resolution Imaging Spectroradiometer (MODIS) MOD10A1 V6.1 snow cover product (Riggs et
326 al., 2015). Snow depth and snow water equivalent were acquired at 1 km spatial resolution from
327 NOAA National Weather Service's SNOw Data Assimilation System (SNODAS) (Barrett, 2004).
328 We computed mean composites for all snow variables during the winter (Dec-Feb).
329

330 For soil properties, we obtained soil pH, texture (sand, silt, clay, and bulk density), volumetric
331 water content, saturated water content, and soil organic matter from the Polaris database (Chaney
332 et al., 2019) available at 30 m resolution. We used the National Elevation Dataset from the
333 NASA Earthdata portal available at 10 m resolution to derive elevation, slope, aspect, hillshade,
334 terrain wetness index, and terrain roughness index. We used a land cover/use map to mask out
335 non-rangeland areas before implementing the regression model to emphasize the habitat of
336 MEOF in the western SD rangelands. The land cover/use data were derived at 30 m resolution
337 from the 2019 National Land Cover Database (NLCD 2019, Dewitz, 2021). We also derived the
338 distance to developed/urban areas, including non-primary roads as a proxy for proximity to
339 roads. Lastly, the distance to stream product was derived from the national hydrography dataset
340 developed by the U.S. Geological Survey National Geospatial Program. All the variables were
341 acquired from the Google Earth Engine (GEE) platform and processed in ArcMap 10.8.1. All
342 variables were resampled to 10 m resolution and projected in Albers Equal Area projection and
343 WGS 84 datum. We used bilinear interpolation for predictor variables to preserve data integrity
344 during resampling. A detailed summary of all the independent variables utilized in this study is
345 provided in Table S5. The method workflow for predicting the invasive yellow sweetclover
346 percent cover for 2016-2023 is illustrated in Figure 2.
347

348 2.6 Regional MEOF cover regression model

349
350 We compiled a total of 22,972 MEOF percent cover samples for the regional-scale regression
351 analysis. After removing duplicate records (samples from different sources falling within the
352 same pixel and year), 20,275 unique samples remained. Most machine learning models such as
353 RFs work on the assumption that the samples are independent and randomly distributed. If this
354 assumption is violated due to spatial autocorrelation, model performance metrics (like accuracy,
355 R^2) can be overestimated (Liu et al., 2022). To deal with this issue, we calculated Global
356 Moran's I with a minimum distance of 50 m on the MEOF percent cover samples to test for
357 spatial autocorrelation between the samples within each year (Moran, 1950). We implemented
358 permutation test for the samples to generate the null distribution and assess the significance of

359 the Moran's I. A 50 m threshold is equivalent to five pixels which helps in mitigating the
360 influence of immediate neighbors, which often exhibit strong spatial autocorrelation due to their
361 proximity. By setting this distance, we aimed at reducing local clustering while ensuring a degree
362 of spatial independence among samples, which is critical for robust estimation of global spatial
363 autocorrelation. Similar buffer distances have been used in previous ecological studies to
364 distinguish between fine-scale spatial dependence and broader spatial patterns, particularly in
365 heterogeneous landscapes where plant cover could be spatially clustered at short ranges
366 (Baumann et al., 2025). We removed the spatially correlated samples and later used 11,235
367 observed samples to develop a generalized percent cover regression model using the RF
368 algorithm. We constructed a predictor variable database by extracting observed sample points
369 from the satellite-derived predictor variables (rasters) for training the RF model. We
370 implemented a spearman correlation coefficient (r) threshold of 0.8 to remove highly correlated
371 predictor variables (Dubuis et al., 2011; Stohlgren et al., 2010; Zar, 2005). We then implemented
372 a Recursive Feature Elimination (RFE) method with 5-repeat, 10-fold cross-validation to
373 determine the top predicting variables (Breiman, 2017; Guyon et al., 2002). The observation
374 samples were split in an 80:20 ratio for training and testing sets using the bootstrap method with
375 replacement. All the variables were scaled and centered before the development of the prediction
376 model. We implemented hyperparameter tuning (*mtry* and *ntrees*) and used the mean absolute
377 error (MAE), mean absolute percentage error (MAPE), root mean square error (RMSE), and the
378 coefficient of determination (R^2) metrics to evaluate the model performance during the testing
379 phase. The MEOF percent cover was predicted using the best generalized model and the best
380 statistical metrics. We used the reference of the habitat suitability map from Saraf et al., (2023)
381 to mask out the low probability of occurrence regions and to develop final MEOF prediction
382 maps. All the analyses were performed using the 'caret' package in the RStudio environment
383 (Kuhn, 2015).

384

385 3. Results

386

387 3.1 Yellow sweetclover cover from UAS imagery

388

389 We used 6,000 training points to train and test an RF classification model by splitting them to an
390 80:20 ratio, obtaining 4,795 training and 1,205 testing samples. The developed RF classification
391 model exhibited an overall accuracy of 98.76% and kappa coefficient of 0.97 in distinguishing
392 flowering MEOF pixels. The confusion matrix for the classification model is provided in Table
393 S6. The RF classification accuracies can be visually validated in three representative UAS sites
394 with MEOF blooms (Figure 3). The estimated area covered with the classified MEOF presence
395 pixels derived from the RF classification model can be found in Table S7. We generated 5,283
396 percent cover samples from UAS, which were divided into 2,736 samples for training sites and
397 the remaining 2,547 samples for validating the RF regression model. The samples were
398 segregated based on ten training and four validation locations. We implemented the jackknifing
399 to calibrate the derived MEOF cover. The cross-validated predictions showed good agreement
400 with the field observed samples with the R^2 of 0.68 and RMSE of 6.24%, suggesting relatively
401 low average prediction error.

402

403 3.2 Regional-scale Random Forest predictions of MEOF cover

404

405 We used the spearman correlation test (r) on all 64 independent variables with a threshold of 0.8
406 and selected 25 predictor variables (Figure S1). We later implemented a recursive feature
407 selection on the 25 predictor variables and selected the 13 top predictor variables. The top 13
408 predictor variables included climatic variables — mean annual precipitation (MAP), coefficient
409 of variation of MAP (MAPcv), mean annual temperature (MAT), coefficient of variation of
410 MAT (MATcv), snow depth (SnowDepth), and coefficient of variation of snow depth
411 (SnowDepth_cv); topographic variables — elevation (Elevation) and slope (Slope); proximity to
412 roads (Dist_Roads); and remote sensing indices capturing moisture and vegetation properties —
413 Normalized Difference Moisture Index (NDMI), coefficient of variation of Normalized
414 Difference Water Index (NDWIcv), coefficient of variation of Land Surface Water Index
415 (LSWIcv), and coefficient of variation of Tasseled Cap Wetness (TCWcv; Table 2). We took the
416 threshold of 0.3 for Moran's I to reduce the positive spatial autocorrelation among the samples.
417 We used sampling with replacement to calculate the significance of the Moran's I. We found that
418 all the years except 2019 and 2023 showed very low spatial autocorrelation with Moran's I of
419 <0.2 (Table S8). We reduced the spatially autocorrelated samples for 2019 and 2023 by selecting
420 samples beyond a minimum distance of 50 m. Overall, we used a total of 11,235 training
421 samples to develop an RF model to predict invasive MEOF cover across western SD. We used
422 80% of these samples (9,006 total) for training and 20% (2,229 total) for testing the model, with
423 3 *mtry* and 1500 *ntrees* as the optimized hyperparameters for the regression model. We noticed
424 that the reduction in sample size had little-to-no effect on the model statistics and metrices. The
425 developed RF model exhibited an R^2 of 0.76, RMSE of 15.11, MAE of 10.95, and MAPE of 1.06
426 %. The predicted cover maps for 2019 and 2023 showed a relatively higher percent cover range
427 than those for other years (Figure S2). The temporal maps showed a higher cover of MEOF in
428 the western counties compared to the eastern counties of western SD (Figure 4). We also found
429 that the western section of the study region, including Butte, Harding, Pennington, Custer, and
430 Fall River counties, were the major hotspots for MEOF cover and showed persistent higher
431 percent cover particularly in 2018, 2019 and 2023. This region tends to have a wider spread of
432 high-density cover over the years. The hotspots were more evident in wet years especially along
433 the floodplains of the Missouri River tributaries, as we move along the west-to-east gradient
434 across western SD. Variable importance showed Normalized Difference Moisture Index (NDMI),
435 proximity to roads (Dist_roads), variability in Normalized Difference Water Index (NDWIcv),
436 and Elevation were the top contributing variables for predicting MEOF cover (Figure S3).
437

438 We created a MEOF percent cover map series for 2016–2023 and compared it with precipitation
439 anomaly maps to assess the potential relationship between MEOF cover and interannual climatic
440 variability. These precipitation anomaly maps showed that the western SD witnessed above-
441 average precipitation in a few regions for 2018 and 2023 and most of the western SD for 2019
442 (Figure S4). The central and eastern counties in 2019 and the central and southern counties in
443 2023 showed a greater range of MEOF covers showing a consistent pattern of MEOF resurgence
444 with the return of wet conditions. Despite 2016 being a relatively normal or slightly dry year,
445 sweetclover cover remained moderate with less spatial variability, indicating less widespread
446 establishment. The widespread establishment of MEOF could be seen increasing in 2018, with a
447 high Coefficient of Variation (CV) of 0.5 and the percent cover reached a peak in the subsequent
448 year of 2019. For the years 2020, 2021 and 2022, most regions experienced average to below-
449 average rainfall conditions. During these years, the MEOF percent cover reached up to 50%,
450 with a sharp drop in percent cover in 2021, where the maximum cover was only 43%. This

451 showed drought conditions likely limit growth and establishment. The year 2020 and 2022 acted
452 as transitional years, possibly due to lagged ecological response. For dry years, the majority of
453 western SD predicted less than 50% cover.

454
455 Overall, we found a high percent cover range in the western counties of western SD including
456 Butte, Meade, Pennington, Custer, Fall River, Jackson, Bennet and Oglala Lakota counties.
457 Central South Dakota counties showed fluctuating trends, with moderate to high coverage in
458 some years (e.g., 2018, 2019, 2023) and relatively low coverage in other years (e.g., 2020, 2021),
459 whereas the eastern counties (i.e., Corson, Dewey, and Stanley) consistently exhibited relatively
460 low percent cover (<20%) for the majority of years. In the eastern region, MEOF appeared to be
461 more scattered and patchier with fewer patches of higher percent cover near floodplains, which
462 are situated at lower elevations and benefit from high moisture availability especially in the years
463 2018 and 2019. During the summer fieldwork of 2022, we observed MEOF predominantly in the
464 first year of its life cycle. In the following year, we observed ample coverage of MEOF blooms
465 in Butte County, SD forming patches substantial enough to be captured by the drones. This
466 temporal pattern arises from the biennial growth period of MEOF. Additionally, we predicted
467 MEOF percent cover estimates for the year 2024 using our trained model (Figure S5). This 2024
468 prediction has been validated with the Planet imagery and is yet to be validated with the field
469 samples. Validation of model performance for 2024 and subsequent years with PlanetScope
470 imagery remains a key focus for future work.

471
472 Year-wise evaluation of model performance revealed considerable variation in normalized
473 RMSE (nRMSE), which ranged from 0.12 in 2022 to 0.65 in 2023 (Table S9). The year-wise
474 sample distribution of observed MEOF cover could be a partial reason for these differences. In
475 2018, the observed cover exhibited the greatest variability (CV = 0.51) and reached a maximum
476 cover of 81%. However, the nRMSE remained low (0.19), indicating that the model effectively
477 captured patterns in years with a broader range of values. Conversely, 2023 exhibited the highest
478 error (nRMSE = 0.657) despite having the 100% maximum cover and the lowest variability (CV
479 = 0.25). This high error occurred despite a relatively large sample size, likely due to spatial
480 clustering and the reduced ability of the model to predict extreme cover values. Consequently,
481 the model's capacity to generalize to high-cover conditions was restricted. Similarly, 2020 had a
482 moderate maximum cover (56%) but relatively high error (nRMSE = 0.55), which may reflect
483 imbalances in sample distribution across cover classes. In contrast, the most optimal overall
484 performance was achieved in 2022 (max = 57%, CV = 0.38) (nRMSE = 0.124), which implies
485 that predictive accuracy is enhanced by balanced sampling across cover ranges. These results
486 emphasize that the distribution and variability of cover values across years have a significant
487 impact on predictive performance, although increasing the sample size improves model stability.

488
489 **4. Discussion**

490
491 4.1 Significance of mapping MEOF superblooms

492
493 Our study offers a workflow for different plant species of annuals, biennials, or geophytes that
494 share dominance during the bloom events, exhibiting huge blooms in specific years with
495 differences of 4 to 10 weeks in their length and peak of the flowering period (Vidiella et al.,
496 1999). These blooms cause a sudden increase in annual net primary production, triggering

497 relevant changes in the ecosystem such as increases in soil nitrogen content due to N-fixation,
498 temporary plant composition modifications, attraction of predators, etc. (Jaksic, 2001), as well as
499 changes in the local climate: an increase in evapotranspiration and a decrease in albedo (He et
500 al., 2017). Various bloom events in arid and semi-arid regions, such as rare blooms in the arid
501 Atacama Desert or superblooms of wildflowers in California's southeastern deserts, have
502 fascinated many researchers and media sources recently (Chávez et al., 2019; Martínez-Harms et
503 al., 2022; Winkler and Brooks, 2020). Our workflow could be useful for detecting and
504 monitoring such events, as well as for managing invasive plant species in grassland ecosystems.
505 Effective management strategies can help mitigate the impact of these invasive species,
506 promoting the health and resilience of grassland ecosystems.
507

508 The occurrence of sweetclover years is predominantly associated with wetter conditions,
509 suggesting that precipitation plays a key role in the resurgence of MEOF (Gucker, 2009). Despite
510 this, climate variables such as annual precipitation or snow depth, did not rank among the top
511 predicting variables. This may be due to MEOF's biennial life cycle, where precipitation from
512 the previous year can influence current-year cover (Klebesadel, 1992; Van Riper and Larson,
513 2009). We tested this by including biennial precipitation (MAP2). However, due to its high
514 correlation with annual precipitation (MAP) and the higher relative importance of MAP, neither
515 variable alone, at the coarser 1 km resolution, adequately captured the biennial dynamics. This
516 unexpected result may be due to the large disparity in spatial resolution between Sentinel-derived
517 variables at 10 m and the 1 km climate variables, which likely contributed to an underestimation
518 of precipitation's importance in the model (Latimer et al., 2006). There is a possibility that
519 MEOF blooms could be influenced not just by precipitation but also by local groundwater
520 availability or soil moisture, particularly in areas near floodplains. While we observed some
521 higher cover near floodplain regions in certain years, the pattern was not consistent across all
522 years. Future analyses focusing on watersheds and hydrological variables could help clarify the
523 environmental drivers of bloom events. Overall, our findings suggest that climate contributes to
524 interannual variation in MEOF cover, while previous studies suggest that spatial heterogeneity
525 and local environmental conditions further modulate vegetation dynamics across the Northern
526 Great Plains (Fore, 2024).
527

528 Despite experiencing ample moisture in some areas in 2016 or 2018, the 'sweetclover year'
529 super blooms were limited only to 2019. This phenomenon may be attributed to MEOF's
530 biennial life cycle, which plays a significant role and acts as a lag effect provided average or
531 above average conditions persist (Van Riper and Larson, 2009). A distinct drop in coverage is
532 seen in the years of 2020 and 2021 across the south, with a recovery in 2022–2023. Moreover,
533 MEOF with >40% percent cover was found in mostly regions that received above-average
534 precipitation during both dry and wet years, highlighting the importance of moisture in
535 regulating dominance. This aligns with previous studies showing that sweetclover cover can
536 fluctuate substantially from year to year, driven by its biennial growth habit and strong
537 germination response in years with high precipitation (Turkington et al., 1978). Although the RF
538 model did not identify precipitation as the top predictor, our predicted MEOF cover maps
539 showed that years of high cover (e.g., 2018 and 2019) coincided with favorable moisture
540 conditions, whereas lower cover in 2020–2021 corresponded with drier years. This pattern
541 supports the hypothesis that 'sweetclover years' of high MEOF abundance occur when favorable

542 moisture conditions are maintained, allowing successful establishment and dominance despite
543 losses from evapotranspiration. These favorable moisture conditions likely facilitate the
544 successful establishment and dominance of MEOF across the Northern Great Plains rangelands,
545 consistent with broader patterns observed for invasive species in semi-arid rangelands (Brooks et
546 al., 2004; D'Antonio and Vitousek, 1992). Similar patterns have been observed for exotic annual
547 grasses such as Cheatgrass (*Bromus tectorum* L.), Red brome (*Bromus rubens* L.) or
548 Medusahead (*Taeniatherum caput-medusae* (L.) Nevski), which often increase under periods of
549 favorable precipitation (Chen and Weber, 2014; Dahal et al., 2023).

550
551 The comprehensive database developed for the invasive MEOF provides a critical foundation for
552 understanding its spatial-temporal invasion dynamics across western SD. The database facilitates
553 detailed analyses of spread dynamics, invasion pathways, and distributional hotspots, thereby
554 improving the ability to model present distribution patterns and project future range expansions
555 under diverse environmental conditions. It also offers a valuable resource for long-term
556 ecological monitoring and adaptive management of MEOF. Furthermore, the database supports
557 investigation of the ecological consequences of MEOF invasion. For example, MEOF's nitrogen-
558 fixing ability may alter soil nutrient dynamics, potentially facilitate its own dominance while
559 affect native plant communities. Increased MEOF cover could lead to declines in native species
560 richness, shifts in plant community composition, and changes in ecosystem processes such as
561 nutrient cycling and primary productivity, particularly in nitrogen-limited prairie ecosystems.
562 Understanding these impacts is critical for predicting long-term vegetation changes and
563 developing targeted management strategies. Beyond immediate applications, this database
564 contributes to a broader understanding of community-level vegetation changes driven by
565 nitrogen-fixing invasive species in grassland environments.

566
567 4.2 Significance of predictor variables
568

569 The variable importance results for MEOF reveals that NDMI is the most influential predictor,
570 indicating that soil and vegetation moisture play a crucial role in supporting its invasion and
571 growth (Figure S2). NDMI characterizes the water stress level in plants (Gao, 1996), which has
572 been used to monitor drought stress and vegetation moisture content (Strashok et al., 2022).
573 Proximity to roads (Dist_roads) emerged as the second most important predictor, explaining the
574 higher cover of MEOF near the roads and its dispersion through road corridors, as MEOF was
575 previously planted along roadsides for soil stabilization (Gucker, 2009). These findings align
576 well with those of Wurtz et al., (2010) who showed that MEOF might have spread onto
577 floodplains from roads, mines, and agricultural fields. This pattern is also consistent with our
578 field survey plots, where a higher percent cover of MEOF was observed closer to roads
579 compared to the interior of plots. Nevertheless, the importance of road proximity should be
580 interpreted cautiously, as greater sampling accessibility near roads may have partially inflated its
581 role in the model. We also found variability in Normalized Difference Water Index (NDWIcv)
582 indicating areas with fluctuating surface water availability may create favourable conditions for
583 MEOF establishment. Furthermore, most climatic variables, such as snow depth, variability in
584 snow depth, mean annual precipitation and Temperature (MAP and MAT), and variability in
585 mean annual precipitation (MAPcv), were found to be of relatively low importance, likely

586 because of their coarser spatial resolutions (500 m and 1 km). Overall, our results suggest that
587 local moisture dynamics, captured by NDMI and NDWICv, and human disturbances, reflected by
588 proximity to roads, are stronger determinants of MEOF distribution at fine spatial scales than
589 coarser-resolution climatic variables (snow depth, MAP, MAT, and their variability). Although
590 climate may establish broad-scale suitability, our data indicate that MEOF invasion patterns in
591 western South Dakota are primarily influenced by local hydrological conditions and human-
592 mediated dispersal.

593

594 4.3 MEOF cover in 2019

595

596 It is important to note that reducing the sample size from 22,972 to 11,235 due to high spatial
597 correlation did not substantially affect model performance. However, in comparison to Saraf et
598 al., (2023), a much larger overall sample size was required to improve predictive accuracy. We
599 developed a single generalized RF model across all years (2016–2023) and applied it to predict
600 MEOF cover annually. Thus, while temporal imbalance in samples (e.g., more samples from
601 bloom years such as 2019 and 2023) influenced the overall distribution of training data, spatial
602 balance and adequate coverage across the full percent cover range were the most critical factors
603 for model accuracy. We found that increasing the sample size and ensuring a more balanced
604 distribution significantly improved model performance, raising R^2 from 0.55 (Saraf et al., 2023)
605 to 0.76. RMSE increased from 7% to 15%, reflecting the inclusion of a wider range of percent
606 cover values rather than insufficient sample size or overall imbalance. Saraf et al., (2023)
607 reported that their model underestimated high percent cover due to a limited sample size ($n =$
608 1,612). In contrast, our model utilized a larger and more evenly distributed sample ($n = 11,235$)
609 across years, improving predictive accuracy and the representation of extreme cover values.
610 These findings suggest that balanced sample sizes enhance both the predictive range and
611 accuracy of RF models, although temporal imbalance in certain years may still influence RMSE
612 and require further investigation. Moreover, it is noteworthy to highlight that it is difficult to
613 fully stratify samples temporally for a biennial species like MEOF, which remains dormant
614 during certain seasons and blooms only under specific environmental conditions.

615

616 Both predicted maps exhibited similar spatial patterns, with higher MEOF cover observed in the
617 western SD counties, such as Butte and Pennington. However, our model predicted a full range
618 of 0-100% cover for 2019, in contrast to the limited range observed in Saraf et al., (2023). This
619 difference is particularly evident in the high MEOF probability areas of western SD rangelands,
620 as shown in Figure 5.

621

622 We conclude that Saraf et al., (2023) significantly underestimated the extent of high percent
623 cover, reporting that areas with > 50% MEOF cover constituted only about 0.76% of SD's total
624 rangelands. In contrast, our updated prediction model estimated that ~12.6% (10,256 km²) of the
625 total rangeland area (81,442 km²) had >50% MEOF cover in 2019. The increase in sample size
626 improved the model ability to predict a wider range of percent cover, providing a more accurate
627 representation of the massive MEOF blooms across western SD in 2019.

628

629 4.4 Uncertainties

630

631 We manually delineated MEOF presence and absence polygons on the UAS imagery, which
632 were used to train and validate the RF classification model. The resulting classified image was
633 then used to derive continuous, wall-to-wall fractional cover estimates across the UAV sites. We
634 used these model-derived continuous MEOF cover values, rather than the manual polygons, for
635 regression analyses in order to generate numerous spatially explicit cover samples and to capture
636 gradients of invasion across the landscape. The UAS orthomosaics in a green-blue-blue band
637 false color combination helped to delineate training polygons. This approach highlighted the
638 potential of multi-spectral bands to easily detect MEOF patches. Furthermore, we randomly
639 sampled 6,000 pixels at 4-6 cm resolution corresponding to the presence and absence of the
640 invasive MEOF. We anticipated that errors might occur during the manual delineation, although
641 the RGB imagery employed in the study displayed the MEOF's characteristic features, such as
642 color, canopy shape, and flowers. The reliability of visual delineation could be compromised in
643 shaded areas. However, the RF classification could accurately distinguish most MEOF pixels
644 from non-MEOF pixels with 98.6%. Visual inspections revealed no discrepancies between the
645 derived percent cover maps at 10 m resolution and submeter resolution MEOF classified maps.
646 This result suggests that any alignment errors were likely minimal and did not significantly affect
647 model accuracy at 10 m resolution especially after calibration of the derived percent cover.
648 While these results are specific to our study area in the Northern Great Plains, the approach has
649 broader implications. We also produced a predictive map for the year 2024 (Figure S5) using the
650 trained model. Assessing the accuracy of the 2024 predictions and extending validation to
651 upcoming future years constitutes an important direction for continued research. Our workflow
652 combined with high-resolution UAS imagery and machine learning can be adapted to other
653 regions with similar vegetation structure and invasion dynamics, offering a scalable and efficient
654 tool for detecting and mapping invasive biennials like MEOF across diverse rangeland
655 ecosystems. Our approach of scaling UAS-derived observations to develop percent cover
656 estimates at broader spatial scales is conceptually similar to Rigge et al., (2020), who
657 demonstrated the utility of integrating high-resolution reference data to improve landscape-scale
658 predictions of rangeland vegetation cover.

659
660 4.5 Validation for 2023 estimates
661

662 We validated the predicted MEOF cover maps using four independent UAS-validation sites.
663 Predictions showed strong correlation with observed MEOF cover derived from UAS imagery,
664 with an R^2 of 0.71, RMSE of 17.81%, MAE of 13.17%, and MAPE of 4.89% (Figure 6, Figure
665 S6). The visual comparison of the predicted maps with UAS imagery at the four validation sites
666 showed that the model generally captured the spatial patterns of MEOF cover. We found that the
667 prediction model underestimated the high percent cover range and overestimated the low to no
668 percent cover regions. In 2023, only 0.76% (621.4 km²) of the total rangeland area (81,442 km²)
669 showed cover exceeding 50%, supporting field observations of widespread MEOF blooms in
670 specific regions. The prominent yellow blooms of MEOF are readily visible in UAS and satellite
671 imagery when found in adequately big clusters, hence supporting the reliability of the model
672 predictions.

673
674 In addition to UAS validation, we used four-band (visible and near-infrared), 3 m resolution
675 Dove Classic and SuperDove PlanetScope (PS) imagery for 2019 and 2023 through the NASA

676 CSDA program (Planet Labs PBC, 2023) to further assess model predictions (Figure 7). PS
677 scenes were selected for locations with predicted high MEOF cover, and false-color
678 combinations (green-green-blue) were applied to enhance visualization of MEOF blooms. These
679 imagery data offered an independent and freely available means to complement the UAS-based
680 validation by visually verifying the spatial patterns of predicted MEOF cover across sites where
681 field data were unavailable. In general, the validation results indicate that the RF model
682 effectively depicts spatial variation in MEOF cover throughout the study area, thereby providing
683 a reliable foundation for evaluating invasion intensity on a landscape scale.

684

685 4.6 Limitations

686

687 Our model does not explicitly incorporate the biennial life cycle of MEOF; rather, we capture
688 this variation indirectly by generating annual time-series maps (2016–2023) that reflect
689 differences in cover between bloom and non-bloom years. Most of the observed MEOF cover
690 samples were collected during the second year of its life cycle to enable capture of its flowering
691 stage. The yellow sweetclover cover peaked during the wetter years (2019 and 2023) as shown in
692 Figure S3, and most of the sampling strength was obtained during these years (Table S1). We
693 used the coefficient of variation to capture the temporal variation of the independent variables
694 during summer (JJA). However, cloud cover of >10% in the region remained the major
695 limitation of this study. Sentinel-2 data provides high temporal resolution, fast data provisioning,
696 and computing infrastructure, making it easier for land managers to track invasive species in
697 real-time. Our model demonstrated high variable importance of high-resolution variables
698 performed better than climate variables due to their coarser resolution. This underperformance of
699 coarser variables suggests the need for higher spatial resolution datasets in mapping invasive
700 plant species. High-resolution mapping, even at Sentinel-2 (10 m) or PlanetScope (3 m)
701 resolution, is complicated by the uneven spatial resolution of independent variables, making it
702 more difficult to understand their relative roles in characterizing the niche of invasive species.
703 Mapping at very high resolution, such as 3 m PlanetScope imagery, has its own limitations,
704 including fewer spectral bands, lower radiometric calibration, and higher noise levels in
705 vegetation indices, which can affect the accuracy of species-specific detection.

706

707 5 Data availability

708

709 The developed invasive MEOF percent cover datasets are freely available at the figshare
710 repository (Saraf et al., 2025) (<https://doi.org/10.6084/m9.figshare.29270759.v1>). The repository has
711 two folders: the first folder named “resampled predicted cover maps” contains predicted percent
712 cover maps of invasive yellow sweetclover resampled at 20m resolution due to size limitations.
713 We can provide the original 10m resolution images upon request. Each file is saved in GeoTiff
714 format in the Albers Conic Equal Area projection. Each file is saved with an acronym of ‘m’ for
715 MEOF followed by an underscore and a year. Missing data are represented by “No data”. The
716 other folder named “sample_code_and_data” contains the R code and an exemplary sample data
717 to predict the MEOF percent cover.

718

719 **6 Conclusions**

720
721 Our integrated approach combining high-resolution UAS imagery, RF classification and
722 regression models, and multi-year satellite and climatic data enabled the effective mapping and
723 monitoring of MEOF cover across western South Dakota. The models demonstrated strong
724 performance with high accuracy in both classification and regression tasks, validating the use of
725 drone-derived percent cover for landscape-scale predictions. The findings highlight the critical
726 role of local moisture availability, proximity to roads, and surface water variability in driving
727 MEOF invasion, while broader climatic variables played a comparatively limited role due to
728 their coarser resolution. Temporal maps revealed that MEOF expansion is closely linked to
729 wetter years, aligning with its biennial life cycle and reinforcing the concept of "sweetclover
730 years." The updated 2019 cover map was significantly improved from the previous estimates,
731 capturing a broader percent cover range and representing invasion hotspots. Validation using
732 2023 UAS sites and PlanetScope imagery further confirmed the model's reliability. PlanetScope
733 imagery provided an independent means to visually assess predicted MEOF cover in areas where
734 drone data are unavailable and served as a complementary source of validation. Our study
735 proposes a workflow of a generalized model that could be applicable to various plant species
736 annuals, biennials, and geophytes that exhibit episodic dominance during bloom events. Our
737 database on MEOF enables analysis of its invasion dynamics, supports predictive modeling of
738 current and future distributions, and informs long-term monitoring and management. It also
739 provides a foundation for assessing ecological impacts on native species and community
740 composition in nitrogen-poor grasslands. Our study also provides a valuable tool for detecting
741 and monitoring superbloom events and can support the management of invasive plant species
742 such as MEOF in grassland ecosystems. Effective management strategies informed by these
743 insights may help mitigate the ecological impacts of invasive species, thereby enhancing the
744 health and resilience of grassland environments.

745 **Code availability**

746 The codes used to produce the multitemporal MEOF maps are publicly available on figshare
747 repository (Saraf et al., 2025) (<https://doi.org/10.6084/m9.figshare.29270759.v1>).

748 **Author contributions**

749 SS – Conceptualization, Data Curation, Formal Analysis, Methodology, Software, Validation,
750 Visualization, and Writing – original draft, review and editing. RJ - Funding acquisition, Project
751 administration, Resources, Supervision, Conceptualization and Writing – review & editing. VK –
752 Data Curation, Visualization, Software, Writing – review and editing. KJ - Data Curation. GH -
753 Visualization, Writing – review and editing. JC - Writing – review and editing. RL - Writing –
754 review and editing.

755 **Acknowledgements**

756 We thank all the institutes, organizations, and developers of the various datasets for making their
757 products freely available. Our appreciation also goes to NASA Commercial SmallSat Data
758 Acquisition (CSDA) program for providing us access with PlanetScope Imagery. We would also
759 like to thank Michele Thornton for providing us Daymet data for 2024 way ahead of its release
760 for us to predict MEOF percent cover for 2024. We acknowledge various funding sources
761

763 including NSF EPSCoR RII: EPSCoR Research Fellows, SDBOR Competitive Research Grant,
764 and the Cable Grant Fellowship, Department of Biology, University of South Dakota. We
765 sincerely thank both anonymous referees for their constructive comments and suggestions, which
766 greatly helped improve the quality of this manuscript.

767

768 Competing interests

769 The contact author has declared that none of the authors has any competing interests.

770

771 References

772 Agnew, W., Uresk, D. W., and Hansen, R. M.: Flora and Fauna Associated with Prairie Dog
773 Colonies and Adjacent Ungrazed Mixed-grass Prairie in Western South Dakota,
774 <https://doi.org/10.2307/3899285>, 1986.

775 Alvarez-Taboada, F., Araújo-Paredes, C., and Julián-Pelaz, J.: Mapping of the Invasive Species
776 Hakea sericea Using Unmanned Aerial Vehicle (UAV) and WorldView-2 Imagery and an
777 Object-Oriented Approach, *Remote Sens.*, 9, 913, <https://doi.org/10.3390/rs9090913>, 2017.

778 Baena, S., Moat, J., Whaley, O., and Boyd, D.: Identifying species from the air: UAVs and the
779 very high resolution challenge for plant conservation, *PLoS One*, 12, e0188714,
780 <https://doi.org/10.1371/journal.pone.0188714>, 2017.

781 Barrett, B.: Snow Data Assimilation System (SNODAS) Data Products at NSIDC, Version 1,
782 Center, Natl. Oper. Hydrol. Remote Sens., <https://doi.org/10.7265/N5TB14TC>, 2004.

783 Baumann, E., Beierkuhnlein, C., Preitauer, A., Schmid, K., and Rudner, M.: Evaluating remote
784 sensing data as a tool to minimize spatial autocorrelation in in-situ vegetation sampling,
785 *Erdkunde*, 79, 25–40, <https://doi.org/10.3112/erdkunde.2025.01.02>, 2025.

786 Bernath-Plaisted, J. S., Ribic, C. A., Hills, W. B., Townsend, P. A., and Zuckerberg, B.:
787 Microclimate complexity in temperate grasslands: implications for conservation and
788 management under climate change, *Environ. Res. Lett.*, 18, <https://doi.org/10.1088/1748-9326/acd4d3>, 2023.

789 Bradley, B. A.: Remote detection of invasive plants: a review of spectral, textural and
790 phenological approaches, *Biol. Invasions*, 16, 1411–1425, <https://doi.org/10.1007/s10530-013-0578-9>, 2014.

791 Breiman, L.: Classification and regression trees, Routledge, 2017.

792 Breiman, L., Friedman, J. H., Olshen, R. A., and Stone, C. ..: Classification And Regression
793 Trees (1st ed.), Routledge, <https://doi.org/https://doi.org/10.1201/9781315139470>, 1984.

794 Brooks, M. L., D'Antonio, C. M., Richardson, D. M., Grace, J. B., Keeley, J. E., DiTomaso, J.
795 M., Hobbs, R. J., Pellatt, M., and Pyke, D.: Effects of invasive alien plants on fire regimes,
796 *Bioscience*, 54, 677–688, [https://doi.org/10.1641/0006-3568\(2004\)054\[0677:EOIAPO\]2.0.CO;2](https://doi.org/10.1641/0006-3568(2004)054[0677:EOIAPO]2.0.CO;2),
797 2004.

798 Chaney, N. W., Minasny, B., Herman, J. D., Nauman, T. W., Brungard, C. W., Morgan, C. L. S.,
799 McBratney, A. B., Wood, E. F., and Yimam, Y.: POLARIS Soil Properties: 30-m Probabilistic
800 Maps of Soil Properties Over the Contiguous United States, *Water Resour. Res.*, 55, 2916–2938,
801 <https://doi.org/10.1029/2018WR022797>, 2019.

802 Chávez, R. O., Moreira-Muñoz, A., Galleguillos, M., Olea, M., Aguayo, J., Latín, A., Aguilera-
803 Betti, I., Muñoz, A. A., and Manríquez, H.: GIMMS NDVI time series reveal the extent,
804 duration, and intensity of “blooming desert” events in the hyper-arid Atacama Desert, Northern
805 Chile, *Int. J. Appl. Earth Obs. Geoinf.*, 76, 193–203,
806 <https://doi.org/https://doi.org/10.1016/j.jag.2018.11.013>, 2019.

809 Chen, F. and Weber, K. T.: Assessing the impact of seasonal precipitation and temperature on
810 vegetation in a grass-dominated rangeland, *Rangel. J.*, 36, 185–190, 2014.

811 Cleland, E. E., Collins, S. L., Dickson, T. L., Farrer, E. C., Gross, K. L., Gherardi, L. A., Hallett,
812 L. M., Hobbs, R. J., Hsu, J. S., Turnbull, L., and Suding, K. N.: Sensitivity of grassland plant
813 community composition to spatial vs. temporal variation in precipitation, *Ecology*, 94, 1687–
814 1696, <https://doi.org/10.1890/12-1006.1>, 2013.

815 Colomina, I. and Molina, P.: Unmanned aerial systems for photogrammetry and remote sensing:
816 A review, *ISPRS J. Photogramm. Remote Sens.*, 92, 79–97,
817 <https://doi.org/10.1016/j.isprsjprs.2014.02.013>, 2014.

818 D'Antonio, C. M. and Vitousek, P. M.: Biological Invasions by Exotic Grasses, the Grass/Fire
819 Cycle, and Global Change, *Annu. Rev. Ecol. Syst.*, 23, 63–87, 1992.

820 Dahal, D., Boyte, S. P., and Oimoen, M. J.: Predicting Exotic Annual Grass Abundance in
821 Rangelands of the Western United States Using Various Precipitation Scenarios, *Rangel. Ecol.*
822 *Manag.*, 90, 221–230, <https://doi.org/10.1016/j.rama.2023.04.011>, 2023.

823 Dewitz, J.: National Land Cover Database (NLCD) 2019 Products, US Geol. Surv. Sioux Falls,
824 SD, USA, <https://doi.org/10.5066/P9KZCM54>, 2021.

825 Dubuis, A., Pottier, J., Rion, V., Pellissier, L., Theurillat, J. P., and Guisan, A.: Predicting spatial
826 patterns of plant species richness: A comparison of direct macroecological and species stacking
827 modelling approaches, *Divers. Distrib.*, 17, 1122–1131, <https://doi.org/10.1111/j.1472-4642.2011.00792.x>, 2011.

828 Fore, S. R.: The Impact of Land Use and Land Cover Change on Vegetation, Ecosystem
829 Dynamics, and Conservation in the Northern Great Plains, The University of North Dakota PP -
830 United States -- North Dakota, United States -- North Dakota, 493 pp., 2024.

831 Gao, B.: NDWI—A normalized difference water index for remote sensing of vegetation liquid
832 water from space, *Remote Sens. Environ.*, 58, 257–266,
833 [https://doi.org/10.1016/S0034-4257\(96\)00067-3](https://doi.org/10.1016/S0034-4257(96)00067-3), 1996.

834 Gascon, F., Bouzinac, C., Thépaut, O., Jung, M., Francesconi, B., Louis, J., Lonjou, V.,
835 Lafrance, B., Massera, S., Gaudel-Vacaresse, A., Languille, F., Alhammoud, B., Viallefont, F.,
836 Pflug, B., Bieniarz, J., Clerc, S., Pessiot, L., Trémas, T., Cadau, E., De Bonis, R., Isola, C.,
837 Martimort, P., and Fernandez, V.: Copernicus Sentinel-2A calibration and products validation
838 status, *Remote Sens.*, 9, <https://doi.org/10.3390/rs9060584>, 2017.

839 Gaskin, J. F., Espeland, E., Johnson, C. D., Larson, D. L., Mangold, J. M., McGee, R. A.,
840 Milner, C., Paudel, S., Pearson, D. E., Perkins, L. B., Prosser, C. W., Runyon, J. B., Sing, S. E.,
841 Sylvain, Z. A., Symstad, A. J., and Tekiela, D. R.: Managing invasive plants on Great Plains
842 grasslands: A discussion of current challenges, *Rangel. Ecol. Manag.*, 78, 235–249,
843 <https://doi.org/10.1016/j.rama.2020.04.003>, 2021.

844 Gränzig, T., Fassnacht, F. E., Kleinschmit, B., and Förster, M.: Mapping the fractional coverage
845 of the invasive shrub *Ulex europaeus* with multi-temporal Sentinel-2 imagery utilizing UAV
846 orthoimages and a new spatial optimization approach, *Int. J. Appl. Earth Obs. Geoinf.*, 96,
847 <https://doi.org/10.1016/j.jag.2020.102281>, 2021.

848 Gucker, C. L.: *Melilotus alba*, *M. officinalis*, U.S. Dep. Agric. For. Serv. Rocky Mt. Res. Station.
849 Fire Sci. Lab., 2009.

850 Guyon, I., Weston, J., Barnhill, S., and Vapnik, V.: Gene Selection for Cancer Classification
851 using Support Vector Machines, *Mach. Learn.*, 46, 389–422,
852 <https://doi.org/10.1023/A:1012487302797>, 2002.

853 He, B., Huang, L., Liu, J., Wang, H., Lü, A., Jiang, W., and Chen, Z.: The observed cooling

855 effect of desert blooms based on high-resolution Moderate Resolution Imaging
856 Spectroradiometer products, *Earth Sp. Sci.*, 4, 247–256,
857 <https://doi.org/https://doi.org/10.1002/2016EA000238>, 2017.

858 Hendrickson, J. R., Sedivec, K. K., Toledo, D., and Printz, J.: Challenges Facing Grasslands
859 in the Northern Great Plains and North Central Region, *Rangelands*, 41, 23–29,
860 <https://doi.org/https://doi.org/10.1016/j.rala.2018.11.002>, 2019.

861 Horstrand, P., Guerra, R., Rodríguez, A., Díaz, M., López, S., and López, J. F.: A UAV Platform
862 Based on a Hyperspectral Sensor for Image Capturing and On-Board Processing, *IEEE Access*,
863 7, 66919–66938, <https://doi.org/10.1109/ACCESS.2019.2913957>, 2019.

864 Jaksic, F. M.: Ecological effects of El Niño in terrestrial ecosystems of western South America,
865 *Ecography* (Cop.), 24, 241–250, <https://doi.org/https://doi.org/10.1111/j.1600-0587.2001.tb00196.x>, 2001.

866 John, R., Chen, J., Giannico, V., Park, H., Xiao, J., Shirkey, G., Ouyang, Z., Shao, C.,
867 Laforteza, R., and Qi, J.: Grassland canopy cover and aboveground biomass in Mongolia and
868 Inner Mongolia: Spatiotemporal estimates and controlling factors, *Remote Sens. Environ.*, 213,
869 34–48, <https://doi.org/10.1016/j.rse.2018.05.002>, 2018.

870 Johnson, J. R. and Larson, G. E.: Grassland Plants of South Dakota and the Northern Great
871 Plains, *Research Bulletins of the South Dakota Agricultural Experiment Station* (1887–2011),
872 764 pp., 1999.

873 Josso, P., Hall, A., Williams, C., Le Bas, T., Lusty, P., and Murton, B.: Application of random-
874 forest machine learning algorithm for mineral predictive mapping of Fe-Mn crusts in the World
875 Ocean, *Ore Geol. Rev.*, 162, 105671,
876 <https://doi.org/https://doi.org/10.1016/j.oregeorev.2023.105671>, 2023.

877 Jurjević, L., Gašparović, M., Milas, A. S., and Balenović, I.: Impact of UAS Image Orientation
878 on Accuracy of Forest Inventory Attributes, *Remote Sens.*, 12,
879 <https://doi.org/10.3390/rs12030404>, 2020.

880 Kan, H., Teng, W., Chen, C., Zhang, G., and Pang, Z.: Establishment of alien invasive plant,
881 yellow sweet clover (*Melilotus officinalis*) at a complex ecosystem distributed with farmlands
882 and wasted lands, <https://doi.org/10.21203/rs.3.rs-2933552/v1>, 2023.

883 Kattenborn, T., Lopatin, J., Förster, M., Braun, A. C., and Fassnacht, F. E.: UAV data as
884 alternative to field sampling to map woody invasive species based on combined Sentinel-1 and
885 Sentinel-2 data, *Remote Sens. Environ.*, 227, 61–73,
886 <https://doi.org/https://doi.org/10.1016/j.rse.2019.03.025>, 2019.

887 Klebesadel, L. J.: Extreme Northern Acclimatization in Biennial Yellow Sweetclover (*Melilotus*
888 *officinalis*) at the Arctic Circle, *School of Agriculture and Land Resources Management*,
889 *Agricultural and Forestry Experiment Station*, 1992.

890 Kuhn, M.: A Short Introduction to the caret Package, *R Found. Stat. Comput.*, 1–10, 2015.

891 Landis, J. R. and Koch, G. G.: The Measurement of Observer Agreement for Categorical Data,
892 *Biometrics*, 33, 159, <https://doi.org/10.2307/2529310>, 1977.

893 Langholz, J.: Global Trends in Private Protected Areas and their Implications for the Northern
894 Great Plains Source : Great Plains, *Gt. Plains Res.*, 20, 9–16, 2010.

895 Larson, E. R., Graham, B. M., Achury, R., Coon, J. J., Daniels, M. K., Gambrell, D. K., Jonassen,
896 K. L., King, G. D., LaRacuente, N., Perrin-Stowe, T. I. N., Reed, E. M., Rice, C. J., Ruzi, S. A.,
897 Thairu, M. W., Wilson, J. C., and Suarez, A. V: From eDNA to citizen science: emerging tools
898 for the early detection of invasive species, *Front. Ecol. Environ.*, 18, 194–202,
899 <https://doi.org/https://doi.org/10.1002/fee.2162>, 2020.

901 Latimer, A. M., Wu, S., Gelfand, A. E., and Silander Jr., J. A.: Building Statistical Models To
902 Analyze Species Distributions, *Ecol. Appl.*, 16, 33–50, [https://doi.org/https://doi.org/10.1890/04-0609](https://doi.org/10.1890/04-0609), 2006.

903

904 Li, L.-Y. and Tsai, C.-C.: Accessing online learning material: Quantitative behavior patterns and
905 their effects on motivation and learning performance, *Comput. Educ.*, 114,
906 <https://doi.org/10.1016/j.compedu.2017.07.007>, 2017.

907 Liu, X., Kounadi, O., and Zurita-Milla, R.: Incorporating Spatial Autocorrelation in Machine
908 Learning Models Using Spatial Lag and Eigenvector Spatial Filtering Features,
909 <https://doi.org/10.3390/ijgi11040242>, 2022.

910 Luo, K., Jahufer, M. Z. Z., Wu, F., Di, H., Zhang, D., Meng, X., Zhang, J., and Wang, Y.:
911 Genotypie variation in a breeding population of yellow sweet clover (*Melilotus officinalis*),
912 *Front. Plant Sci.*, 7, 1–10, <https://doi.org/10.3389/fpls.2016.00972>, 2016.

913 Martínez-Harms, J., Guerrero, P., Martínez-Harms, M., Poblete, N., González, K., Stavenga, D.,
914 and Vorobyev, M.: Mechanisms of flower coloring and eco-evolutionary implications of massive
915 blooming events in the Atacama Desert, *Front. Ecol. Evol.*, 10,
916 <https://doi.org/10.3389/fevo.2022.957318>, 2022.

917 Martins, J., Richardson, D. M., Henriques, R., Marchante, E., Marchante, H., Alves, P., Gaertner,
918 M., Honrado, J. P., and Vicente, J. R.: A multi-scale modelling framework to guide management
919 of plant invasions in a transboundary context, *For. Ecosyst.*, 3, <https://doi.org/10.1186/s40663-016-0073-8>, 2016.

920

921 Mayr, S., Kuenzer, C., Gessner, U., Klein, I., and Rutzinger, M.: Validation of Earth Observation
922 Time-Series: A Review for Large-Area and Temporally Dense Land Surface Products, *Remote
923 Sens.*, 11, 2616, <https://doi.org/10.3390/rs11222616>, 2019.

924 Moran, P. A. P.: Notes on Continuous Stochastic Phenomena, *Biometrika*, 37(2), 17–29, 1950.

925 Mouta, N., Silva, R., Pinto, E. M., Vaz, A. S., Alonso, J. M., Gonçalves, J. F., Honrado, J., and
926 Vicente, J. R.: Sentinel-2 Time Series and Classifier Fusion to Map an Aquatic Invasive Plant
927 Species along a River—The Case of Water-Hyacinth, *Remote Sens.*, 15,
928 <https://doi.org/10.3390/rs15133248>, 2023.

929 Müllerová, J., Brůna, J., Bartaloš, T., Dvořák, P., Vítková, M., and Pyšek, P.: Timing Is
930 Important: Unmanned Aircraft vs. Satellite Imagery in Plant Invasion Monitoring, *Front. Plant
931 Sci.*, 8, 1–13, <https://doi.org/10.3389/fpls.2017.00887>, 2017.

932 Owensby, C. E. and Launchbaugh, J. L.: Controlling prairie threeawn (*Aristida oligantha*
933 Michx.) in central and eastern Kansas with fall burning, *J. Range Manag.*, 30, 337–339, 1977.

934 Padró, J.-C., Muñoz, F.-J., Planas, J., and Pons, X.: Comparison of four UAV georeferencing
935 methods for environmental monitoring purposes focusing on the combined use with airborne and
936 satellite remote sensing platforms, *Int. J. Appl. Earth Obs. Geoinf.*, 75, 130–140,
937 <https://doi.org/https://doi.org/10.1016/j.jag.2018.10.018>, 2019.

938 Paul, M., Rajib, A., and Ahiablame, L.: Spatial and Temporal Evaluation of Hydrological
939 Response to Climate and Land Use Change in Three South Dakota Watersheds, *JAWRA J. Am.
940 Water Resour. Assoc.*, 53, <https://doi.org/10.1111/1752-1688.12483>, 2016.

941 Pix4D S.A.: Pix4Dmapper. Version 4.8, www.pix4d.com, 2022.

942 Preston, T. M., Johnston, A. N., Ebenhoch, K. G., and Diehl, R. H.: Beyond presence mapping:
943 predicting fractional cover of non-native vegetation in Sentinel-2 imagery using an ensemble of
944 MaxEnt models, *Remote Sens. Ecol. Conserv.*, 9, 512–526, <https://doi.org/10.1002/rse2.325>,
945 2023.

946 Rai, P. and Singh, J. S.: Invasive alien plant species: Their impact on environment, ecosystem

947 services and human health, *Ecol. Indic.*, 2020, 20 pages,
948 <https://doi.org/10.1016/j.ecolind.2019.106020>, 2020.

949 Rakotoarivony, M. N. A., Gholizadeh, H., Hammond, W. M., Hassani, K., Joshi, O., Hamilton,
950 R. G., Fuhlendorf, S. D., Trowbridge, A. M., and Adams, H. D.: Detecting the invasive
951 *Lespedeza cuneata* in grasslands using commercial small satellite imagery, *Int. J. Remote Sens.*,
952 44, 6802–6824, <https://doi.org/10.1080/01431161.2023.2275321>, 2023.

953 Van Rees, C. B., Hand, B. K., Carter, S. C., Bargeron, C., Cline, T. J., Daniel, W., Ferrante, J.
954 A., Gaddis, K., Hunter, M. E., Jarnevich, C. S., McGeoch, M. A., Morisette, J. T., Neilson, M.
955 E., Roy, H. E., Rozance, M. A., Sepulveda, A., Wallace, R. D., Whited, D., Wilcox, T., Kimball,
956 J. S., and Luikart, G.: A framework to integrate innovations in invasion science for proactive
957 management, *Biol. Rev.*, 97, 1712–1735, <https://doi.org/10.1111/brv.12859>, 2022.

958 Reinhart, K. O., Rinella, M. J., Waterman, R. C., Petersen, M. K., and Vermeire, L. T.: Testing
959 rangeland health theory in the Northern Great Plains, *J. Appl. Ecol.*, 56, 319–329, 2019.

960 Rigge, M., Homer, C., Cleeves, L., Meyer, D. K., Bunde, B., Shi, H., Xian, G., Schell, S., and
961 Bobo, M.: Quantifying Western U.S. Rangelands as Fractional Components with Multi-
962 Resolution Remote Sensing and In Situ Data, <https://doi.org/10.3390/rs12030412>, 2020.

963 Riggs, G. A., Hall, D. K., Román, M. O., and others: MODIS snow products collection 6 user
964 guide, Natl. Snow Ice Data Cent. Boulder, CO, USA, 66, 2015.

965 Van Riper, L. C. and Larson, D. L.: Role of invasive *Melilotus officinalis* in two native plant
966 communities, *Plant Ecol.*, 200, 129–139, <https://doi.org/10.1007/s11258-008-9438-6>, 2009.

967 Sanderson, M., Liebig, M., Hendrickson, J. R., Kronberg, S., Toledo, D., Derner, J., and Reeves,
968 J.: Long-term agroecosystem research on northern Great Plains mixed grass prairie near Mandan,
969 North Dakota, *Can. J. Plant Sci.*, 95, 150810114732003, <https://doi.org/10.4141/CJPS-2015-117>,
970 2015.

971 Saraf, S., John, R., Goljani Amirkhiz, R., Kolluru, V., Jain, K., Rigge, M., Giannico, V., Boyte,
972 S., Chen, J., Henebry, G., Jarchow, M., and Laforteza, R.: Biophysical drivers for predicting the
973 distribution and abundance of invasive yellow sweetclover in the Northern Great Plains, *Landsc.
974 Ecol.*, 38, 1463–1479, <https://doi.org/10.1007/s10980-023-01613-1>, 2023.

975 Saraf, S., John, R., Kolluru, V., Jain, K., Henebry, G., Chen, J., and Laforteza, R.:
976 Spatiotemporal mapping of invasive yellow sweetclover blooms using Sentinel-2 and high-
977 resolution drone imagery, <https://doi.org/10.6084/m9.figshare.29270759>, 2025.

978 Spiess, J., McGranahan, D., Geaumont, B., Sedivec, K., Lakey, M., Berti, M., Hovick, T., and
979 Limb, R.: Patch-Burning Buffers Forage Resources and Livestock Performance to Mitigate
980 Drought in the Northern Great Plains, *Rangel. Ecol. Manag.*, 73,
981 <https://doi.org/10.1016/j.rama.2020.03.003>, 2020.

982 Steen, V. A., Tingley, M. W., Paton, P. W. C., and Elphick, C. S.: Spatial thinning and class
983 balancing: Key choices lead to variation in the performance of species distribution models with
984 citizen science data, *Methods Ecol. Evol.*, 12, 216–226,
985 <https://doi.org/https://doi.org/10.1111/2041-210X.13525>, 2021.

986 Stohlgren, T. J., Ma, P., Kumar, S., Rocca, M., Morisette, J. T., Jarnevich, C. S., and Benson, N.:
987 Ensemble habitat mapping of invasive plant species, *Risk Anal.*, 30, 224–235,
988 <https://doi.org/10.1111/j.1539-6924.2009.01343.x>, 2010.

989 Strashok, O., Ziemiańska, M., and Strashok, V.: Evaluation and Correlation of Sentinel-2 NDVI
990 and NDMI in Kyiv (2017-2021), *J. Ecol. Eng.*, 23, 212–218,
991 <https://doi.org/10.12911/22998993/151884>, 2022.

992 Sulik, J. J. and Long, D. S.: Spectral considerations for modeling yield of canola, *Remote Sens.*

993 Environ., 184, 161–174, [https://doi.org/https://doi.org/10.1016/j.rse.2016.06.016](https://doi.org/10.1016/j.rse.2016.06.016), 2016.

994 Thornton, M. M., Shrestha, R., Wei, Y., Thornton, P. E., and Kao, S.-C.: Daymet: Monthly

995 Climate Summaries on a 1-km Grid for North America, Version 4 R1,

996 <https://doi.org/10.3334/ORNLDAA/2131>, 2022.

997 Trimble Inc. (n.d.): Trimble DA2 GNSS Receiver,

998 <https://geospatial.trimble.com/en/products/hardware/trimble-da2>, 2025.

999 Turkington, R. A., Cavers, P. B., and Rempel, E.: The Biology of Canadian Weeds.: 29.

1000 Melilotus alba Desr. and M. officinalis (L.) Lam., Can. J. Plant Sci., 58, 523–537,

1001 <https://doi.org/10.4141/cjps78-078>, 1978.

1002 Turner, D. and Wallace, L.: Direct Georeferencing of Ultrahigh-Resolution UAV Imagery, IEEE

1003 Trans. Geosci. Remote Sens., 52, <https://doi.org/10.1109/TGRS.2013.2265295>, 2013.

1004 Varner, C.: Invasive Flora of the West Coast: British Columbia and the Pacific Northwest,

1005 Heritage House Publishing Co., University of Washington Press, 2022.

1006 Vidiella, P. E., Armesto, J. J., and Gutiérrez, J. R.: Vegetation changes and sequential flowering

1007 after rain in the southern Atacama Desert, J. Arid Environ., 43, 449–458,

1008 [https://doi.org/https://doi.org/10.1006/jare.1999.0565](https://doi.org/10.1006/jare.1999.0565), 1999.

1009 Winkler, D. E. and Brooks, E.: Tracing Extremes across Iconic Desert Landscapes: Socio-

1010 Ecological and Cultural Responses to Climate Change, Water Scarcity, and Wildflower

1011 Superblooms, Hum. Ecol., 48, 211–223, <https://doi.org/10.1007/s10745-020-00145-5>, 2020.

1012 Wolf, J. J., Beatty, S. W., and Carey, G.: Invasion by Sweet Clover (Melilotus) in Montane

1013 Grasslands, Rocky Mountain National Park, Ann. Assoc. Am. Geogr., 93, 531–543,

1014 <https://doi.org/10.1111/1467-8306.9303001>, 2003.

1015 Wolter, K. M.: The Jackknife Method BT - Introduction to Variance Estimation, edited by:

1016 Wolter, K. M., Springer New York, New York, NY, 151–193, https://doi.org/10.1007/978-0-387-35099-8_4, 2007.

1017 Wurtz, T. L., Macander, M. J., and Spellman, B. T.: Spread of Invasive Plants From Roads to

1018 River Systems in Alaska: A Network Model, U S For. Serv. Pacific Northwest Res. Stn. Gen.

1019 Tech. Rep. PNW-GTR, 699–708, 2010.

1020 Zar, J. H.: Spearman rank correlation, Encycl. Biostat. Wiley Online Libr., 7, 2005.

1021 Zhang, Z., Bao, T., Hautier, Y., Yang, J., Liu, Z., and Qing, H.: Microclimate complexity in

1022 temperate grasslands: implications for conservation and management under climate change,

1023 Ecol. Evol., 12, e9385, [https://doi.org/https://doi.org/10.1002/ece3.9385](https://doi.org/10.1002/ece3.9385), 2022.

1024

1025

1026 **Tables and Figures**

1027

1028 Table 1. Details of the drone flights covered in sample collection for summer 2023.

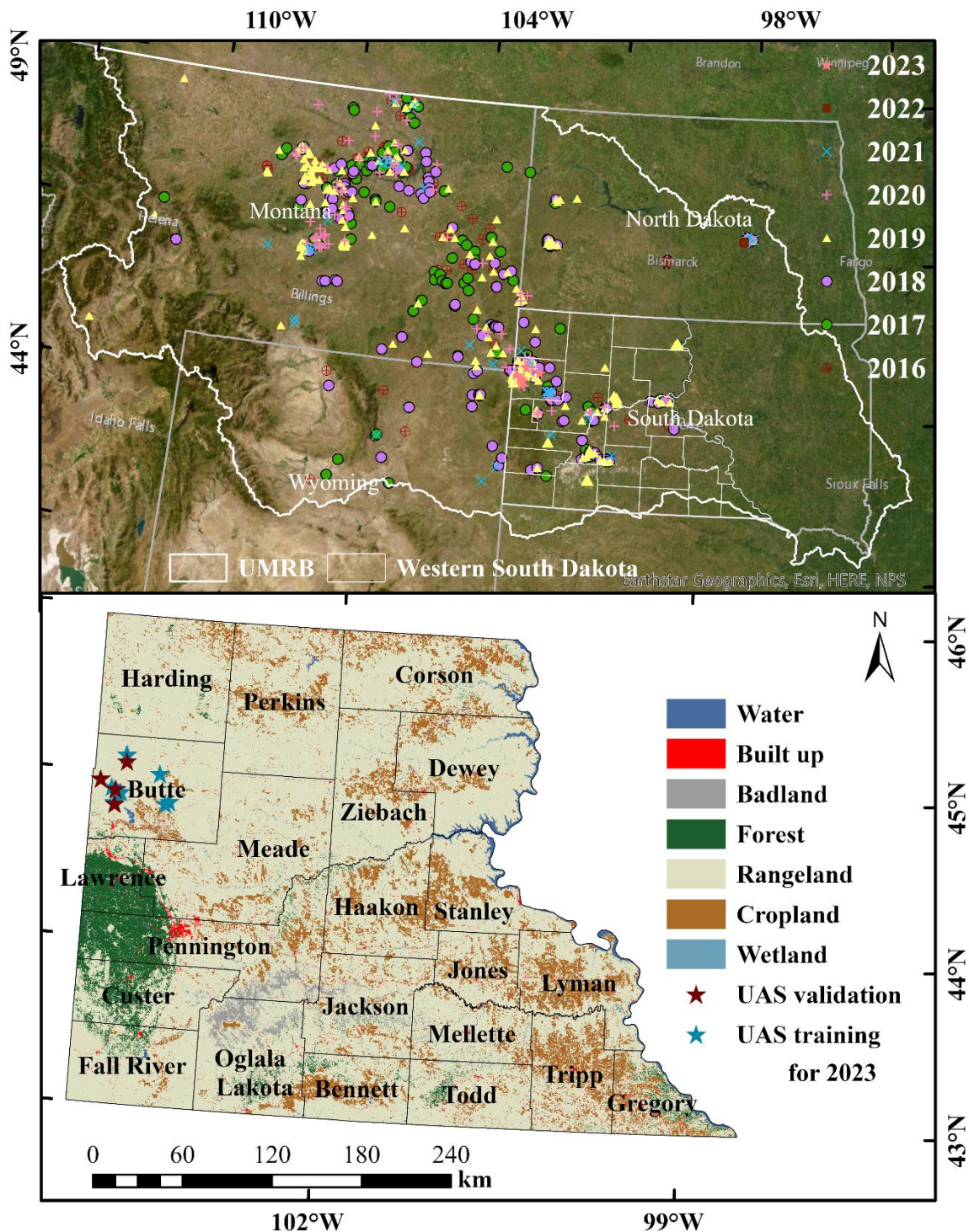
Site	Date	Spatial Resolution (m)	Area (ha)	Sampling
1	July 9	0.06	10.5	Validation
2	July 9	0.03	1.9	Training
3	July 10	0.04	4.9	Training
4	July 10	0.04	4.1	Training
5	July 11	0.07	30.5	Training
6	July 11	0.04	3.2	Training
7	July 12	0.05	7.2	Training
8	July 12	0.03	3	Training
9	July 13	0.04	4.9	Validation
10	July 13	0.04	4.6	Validation
11	July 14	0.03	4.2	Training
12	July 14	0.05	7.2	Training
13	July 15	0.05	10.5	Training
14	July 15	0.04	4.7	Validation

1029

1030 Table 2. Description of 13 independent variables selected for estimating the yellow sweetclover
 1031 cover (%)

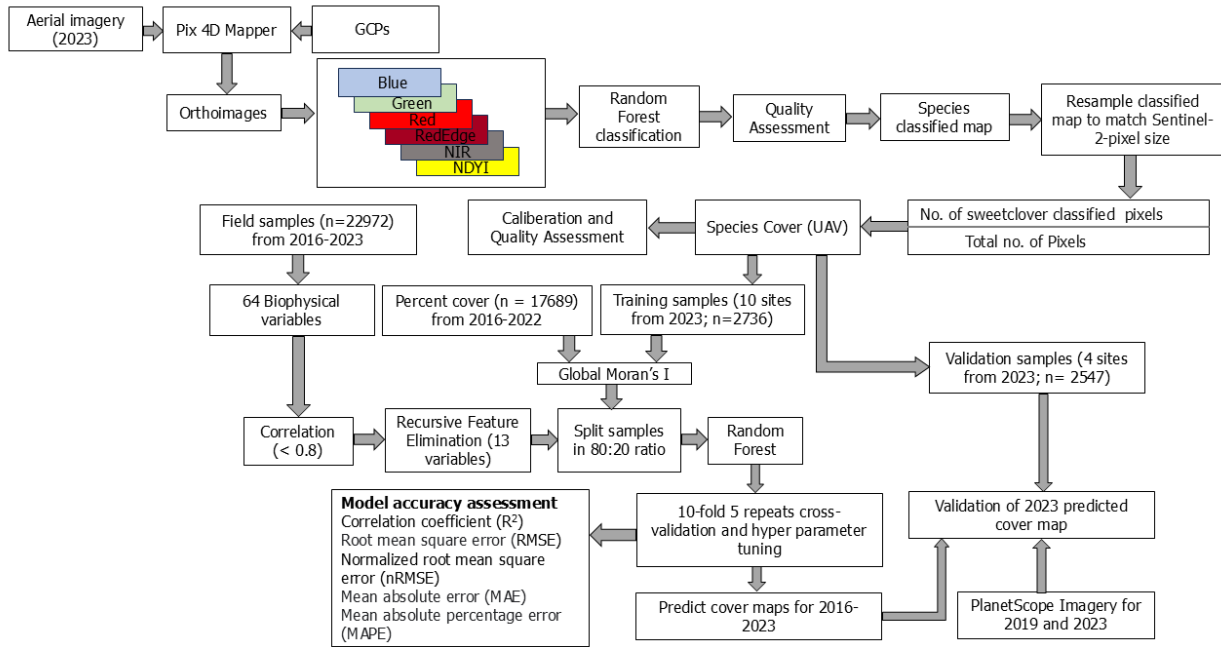
S.No	Independent Variables	Codes	Resolution
1	Mean annual precipitation	MAP	1 km
2	Mean annual precipitation (coefficient of variation)	MAPcv	1 km
3	Mean annual temperature	MAT	1 km
4	Mean annual precipitation (coefficient of variation)	MATcv	1 km
5	Snow Depth	SnowDepth	500m
6	Snow Depth (coefficient of variation)	SnowDepth_cv	500m
7	Elevation	Elevation	10m
8	Slope	Slope	10m
9	Proximity to roads	Dist_Roads	30m
10	Normalized Difference Moisture Index	NDMI	10m
11	Normalized Difference Water Index (coefficient of variation)	NDWIcv	10m
12	Land Surface Water Index (coefficient of variation)	LSWIcv	10m
13	Tasseled Cap Wetness (coefficient of variation)	TCWcv	10m

1032



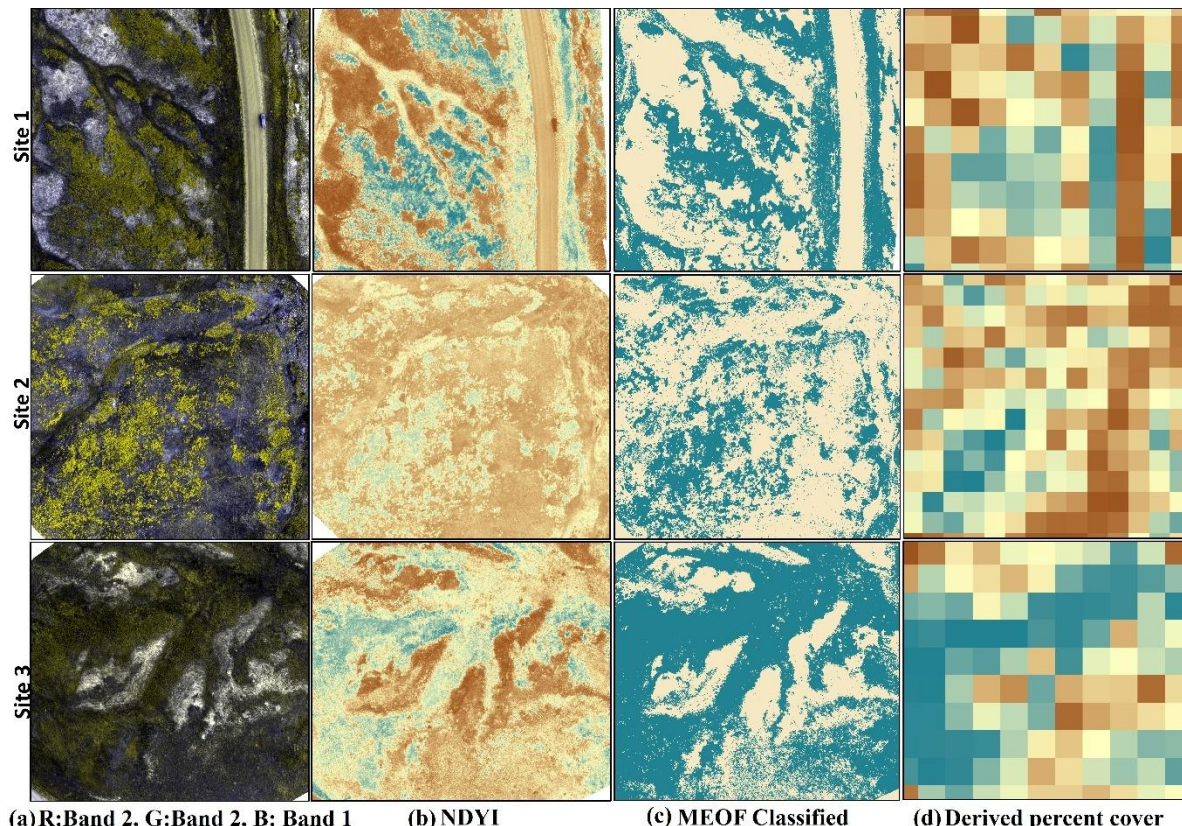
1033
1034
1035
1036
1037
1038
1039

Figure 1 The top panel shows field observations used in this study ($n = 22,972$) collected from 2016 to 2023 across the Northern Great Plains, including our own surveys as well as publicly available datasets such as BLM AIM and NEON (© Esri, Maxar, Earthstar Geographics, and the GIS User Community). The bottom panel shows the UAS training and validation sites overlaid on the National Land Cover Database (NLCD, 2019) land cover map with county boundaries of western South Dakota.

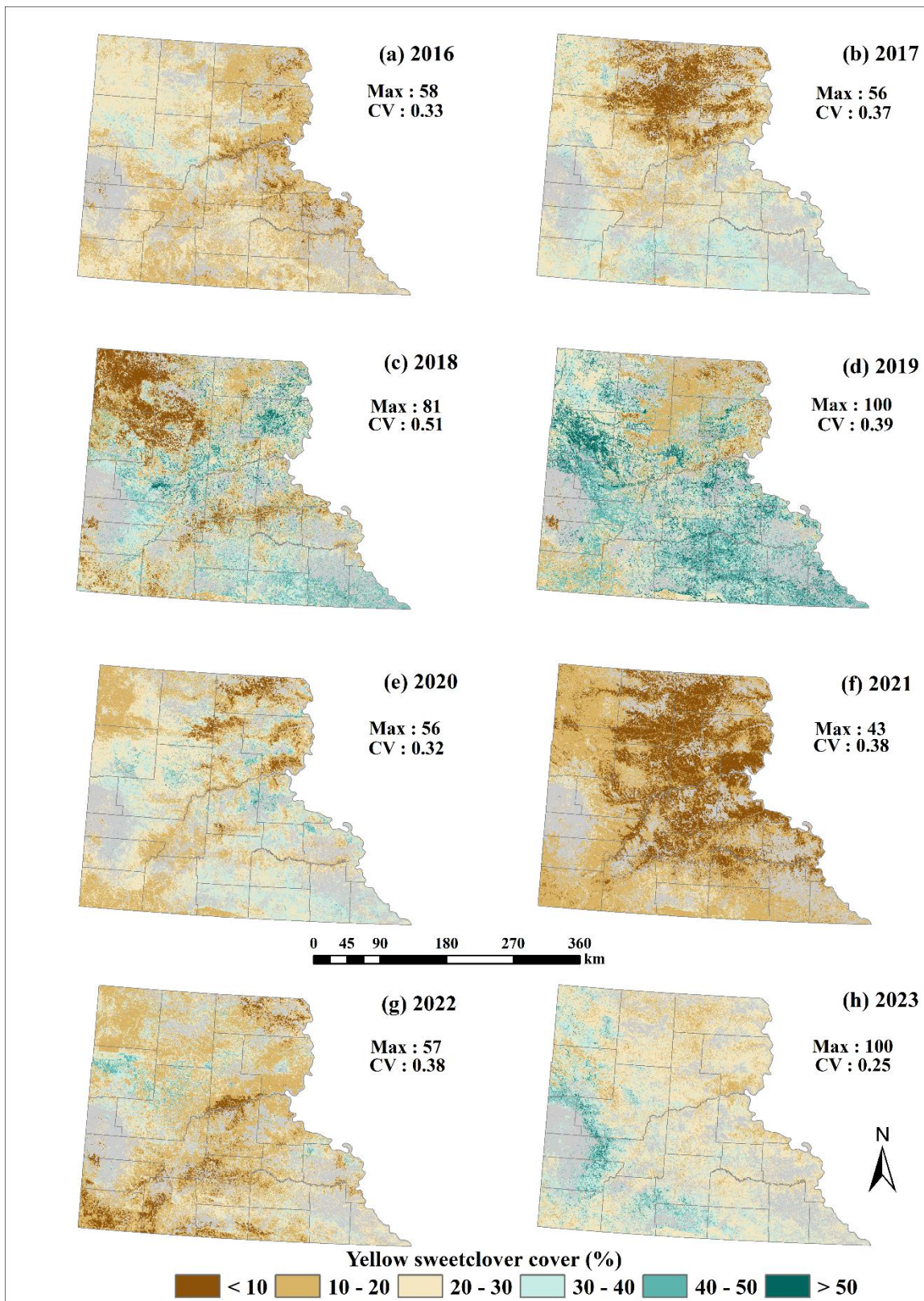


1040
1041
1042

Figure 2 Workflow to predict invasive yellow sweetclover percent cover at 10m resolution using UAS and ancillary data for 2016-2023.



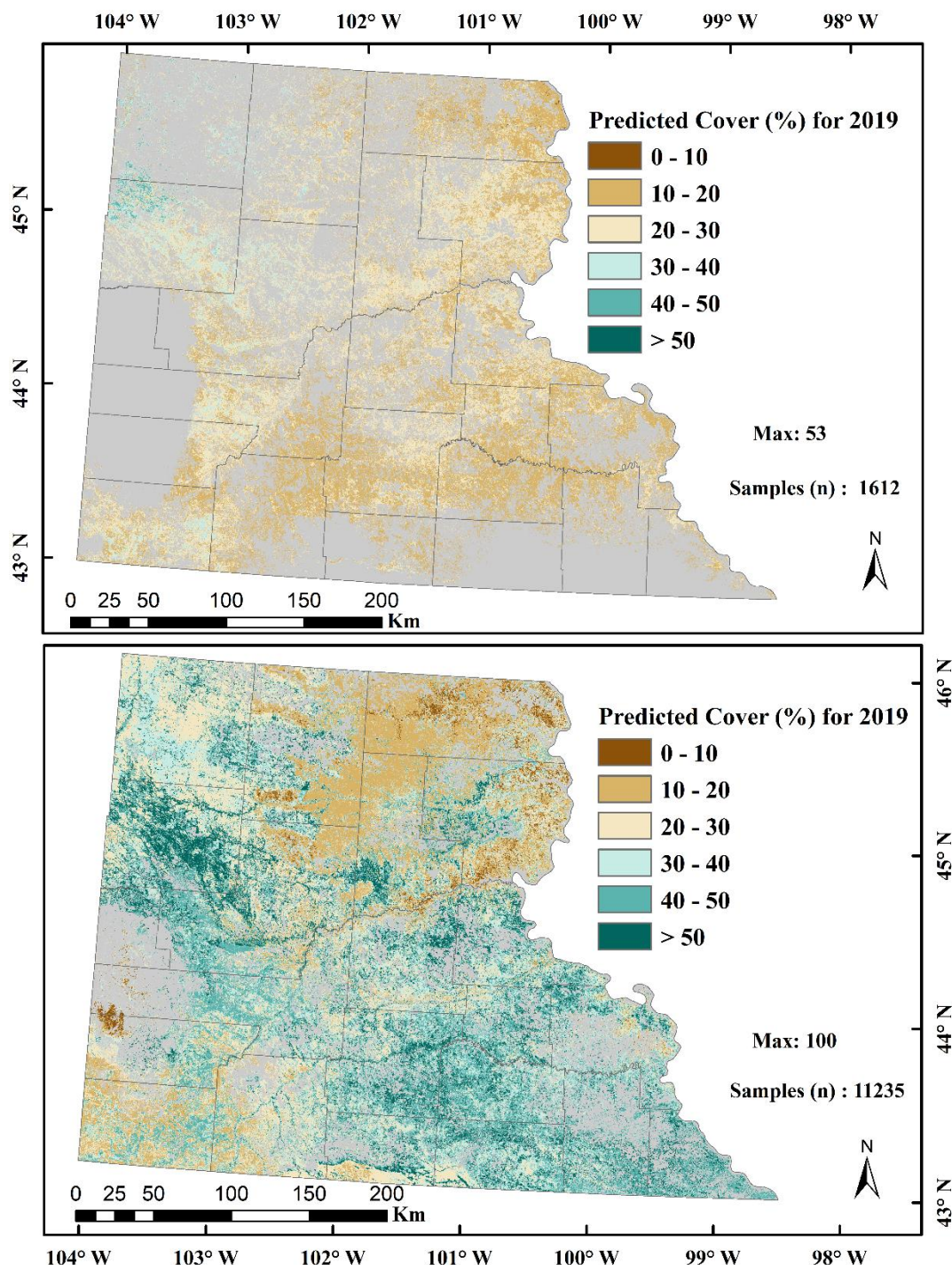
1043
1044 Figure 3 Representative figures for three Unmanned Aerial Systems (UAS) sites with yellow
1045 sweetclover (MEOF) blooms (a) UAS orthoimages in green, green and blue band combination
1046 (b) Normalized Difference Yellowness Index (c) Random Forest classified image showing
1047 yellow sweetclover presence and absence (d) yellow sweetclover cover derived at 10m pixel
1048 size.



1049
1050
1051

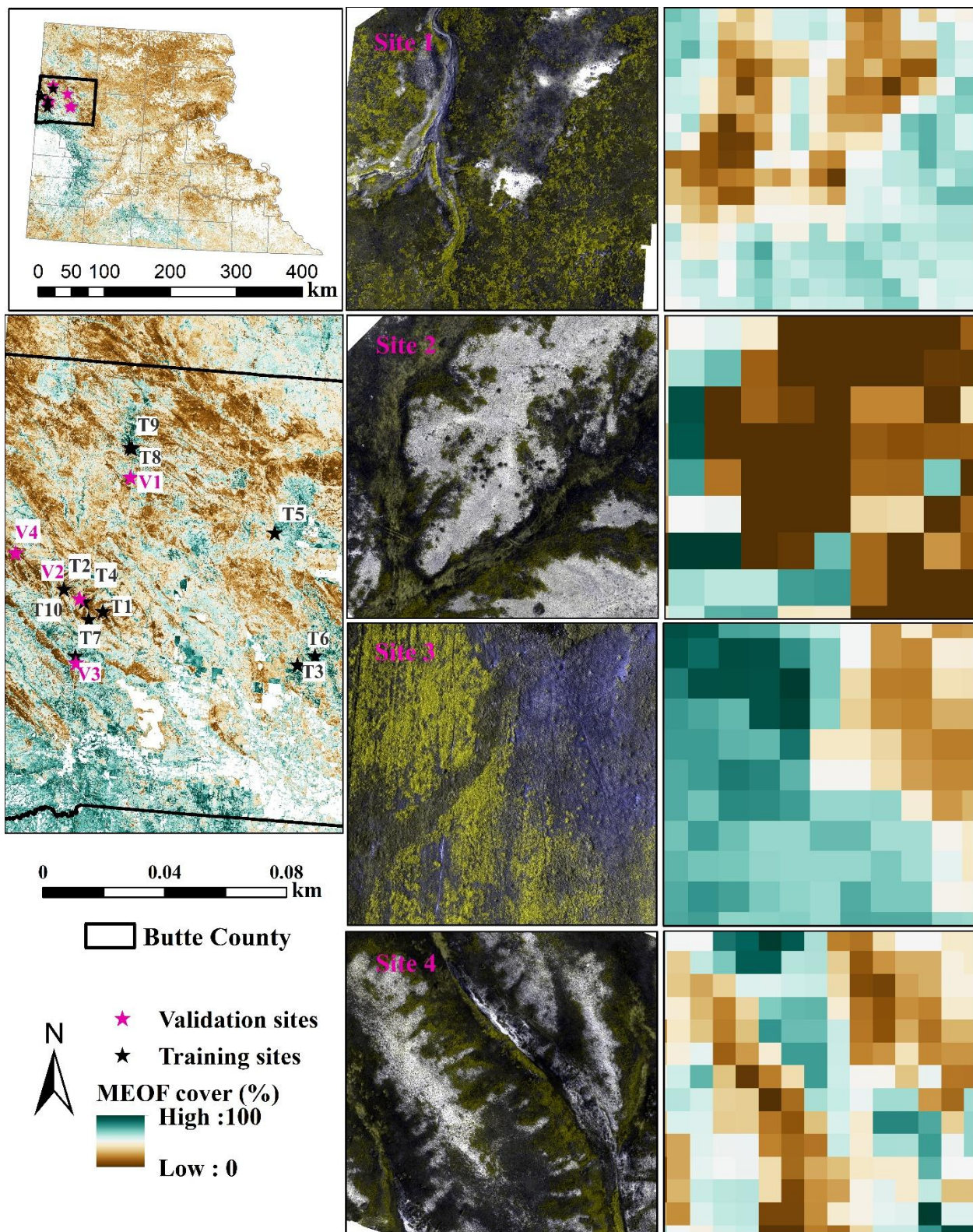
Figure 4 Predicted yellow sweetclover distribution using a generalized Random Forest (RF) regression model for 2016-2023.

1052



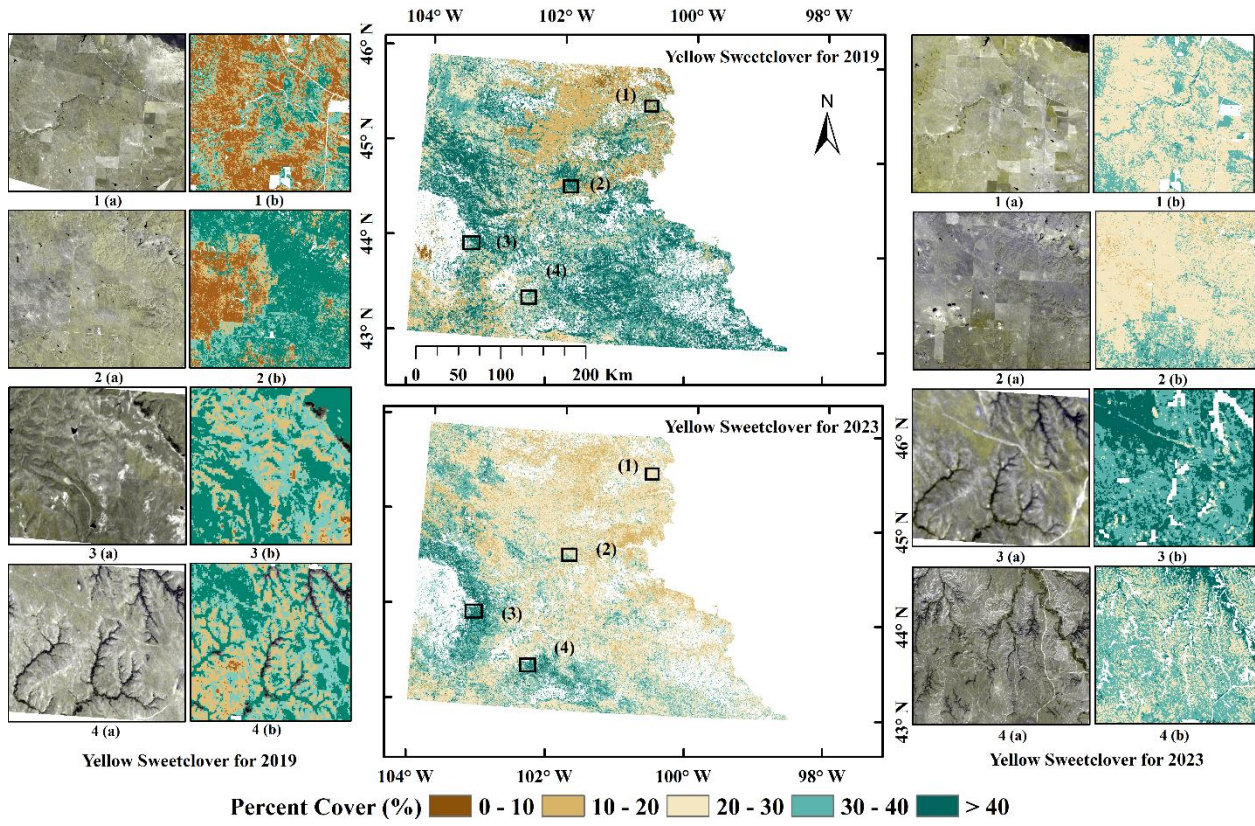
1053

1054 Figure 5. Comparison of yellow sweetclover (*Melilotus officinalis*) cover in western South
 1055 Dakotas for 2019. (a) Percent cover estimates from Saraf et al. (2023) based on 1,612
 1056 samples, showing areas with high probability of yellow sweetclover occurrence. (b) Predicted
 1057 percent cover from the current study using 11,235 samples, highlighting the updated yellow
 1058 sweetclover cover estimates compared with Saraf et al. (2023).



1059

1060 Figure 6. Percent cover estimates for invasive yellow sweetclover for four independent UAS
 1061 validation sites shown in green-green-blue false color combination to highlight yellow
 1062 sweetclover blooms.



1063

1064 Figure 7. Predicted percent cover estimates for invasive yellow sweetclover (MEOF) at four
 1065 different sites represented with numbers for 2019 (left) and 2023 (right). In each site, (a) 3 m
 1066 resolution PlanetScope imagery shown in green, green, and blue band combination to highlight
 1067 yellow sweetclover blooms, and (b) fractional cover of MEOF. (PlanetScope imagery © Planet
 1068 Labs PBC).